# High Energy Physics Latinamerican–European Network fellowship

**Andrés Cimmarusti**

**Universidad de Los Andes, Mérida (Venezuela)**

**Analysis of top anti–top decays in the lepton plus jets channel at the ATLAS experiment**

*Laboratoire de Physique Nucléaire et de Hautes Energies de Paris ; CNRS–IN2P3 ; Université Pierre et Marie Curie–Paris 6 ; Université Denis Diderot–Paris7*

# Contents

# 1  Abstract

Particle physics includes all the experimental research aimed at advancing in the understanding of quarks (the components of protons and neutrons) and leptons (such as electrons), as well as their mutual interactions. The study of the properties of the top quark, the heaviest of the six known quarks, in particular its mass, is of uttermost importance as it may give clues on the origin of the mass difference between the particles and indicate the existence of physics beyond the Standard Model of particle physics. At the start of the Large Hadron Collider at CERN in 2007, the top quark will be produced with large statistics. The ATLAS experiment will have the possibility to study its properties in great detail.

The top quark is an instable particle that decays almost instantaneously and exclusively into a $b$ quark and a $W$ boson, which in turn form jets of stable particles. The precision in the measurement of top quark properties will be limited by the knowledge of some of the detector performances, such as the precision to which the particle energies are measured, or the efficiency with which we can identify some of these particles. The preparation of physics analyses requires the best knowledge of detectors and physics simulation.

I have worked during my internship at the LPNHE Paris on the preparation of two physics analyses on simulated data. A first study has been performed, corresponding to the commissioning phase of the detector with the first data. It has been shown that in ATLAS the top quark can be easily reconstructed, even using a very simple selection and without fulfilling requirements such as flavor tagging or jet energy reconstruction. A second analysis has been performed after the detector and the data were understood. The background due to jets misidentified in the detector as electrons has been studied and found to be negligible. The mass reconstruction performance has been studied for different selections of the final state of the top quark decay. The statistical uncertainty on it will become negligible after a few weeks of data taking compared to the uncertainties related to the jet energy reconstruction. These analyses are a first step for the LPNHE group in their development of physics analyses for the top quark mass measurement.

# 2 The Standard Model

The main goal of particle physics is to increase our knowledge of quarks (the constituents of neutrons, protons and other hadrons), leptons (like the electron) and the interactions which govern them. These particles are until now considered as the building blocks of matter. The linked breakthroughs in both theory and experiment have led to what is now called the "Standard Model". This model describes the contents of the universe with 12 elementary constituents and successfully explains all fundamental interactions save gravitation. Electroweak interaction is the result of the unification of the electromagnetic and weak interactions, carried by the photon $\gamma$ and the vector bosons $W^\pm$ and $Z$, respectively. The gluons carry the strong interaction which is responsible for the cohesion of the nucleus.

## 2.1 Particle Organization

According to the Standard Model the elementary particles are organized in 3 families (see table 1):

- *Radiation quanta:* Each interaction is the result of an exchange of these particles. They are the photon for the electromagnetic force, the vector bosons $Z^0$, $W^+$ and $W^-$ for the weak force and the gluon for the strong force. All the members of this family are bosons, which means they have integer spin values.

- *Matter particles:* these particles are all fermions with spin 1/2. Their number has been determined experimentally. There are 2 types: leptons, subjects to all interactions save the strong one and quarks which interact by any means. These particles are organized in 3 families, each one being composed of a lepton negatively charged (electron, muon, tau) with its corresponding neutrino and 2 quarks, one with a charge of 2/3 and the other -1/3 (1 is considered as the charge of the electron).

- *Higgs boson:* This particle, which has not yet been observed, should be, according to the Standard Model, the responsible for the diverse mass values of the matter particles[1].

| | | | | |
|---|---|---|---|---|
| Fermions | Quarks | $\begin{pmatrix} \text{up } u \\ \text{down } d \end{pmatrix}$ | $\begin{pmatrix} \text{charm } c \\ \text{strange } s \end{pmatrix}$ | $\begin{pmatrix} \text{top } t \\ \text{bottom } b \end{pmatrix}$ |
| | Leptons | $\begin{pmatrix} \text{neutrino } \nu_e \\ \text{electron } e^- \end{pmatrix}$ | $\begin{pmatrix} \text{neutrino } \nu_\mu \\ \text{mu } \mu \end{pmatrix}$ | $\begin{pmatrix} \text{neutrino } \nu_\tau \\ \text{tau } \tau \end{pmatrix}$ |
| Bosons | Gauge Bosons | photon $\gamma$ – electromagnetic force | | |
| | | Vector Bosons $W^\pm$, $Z^0$ – weak force | | |
| | | gluons $g$ – strong force | | |
| | | Higgs boson $H$ ? | | |

Table 1: Standard Model particles

---

[1]Within the frame of quantum electrodynamics photons are always found to have mass equal to zero and since the range of interaction is inversely proportional to the mass of the interaction carrier particle, this gives an infinite range for the electromagnetic force. However this contrasts with the finite ranges for the strong and weak forces, therefore it is thought the origin of the mass of particles is due to a symmetry breaking, which is why the Higgs field is introduced.

## 2.2 Unanswered questions

This model has not yet been proved wrong by experiments, nevertheless we know it is not the final theory for particle physics, because, in its actual form, it does not provide several important answers:

- How can we unify the electroweak interaction with the strong and gravitational interaction? The high number of fundamental parameters[2] represents a hint as to why we have started thinking the Standard Model is just a part of a larger model. SuperSymmetry is one of the most popular extensions. It predicts, among other things, the existence of the so–called supersymmetric particles, counterparts of the particles which constitute ordinary matter.

- At the beginning, the universe contained matter and anti–matter in equal amounts. Why did the anti–matter disappear? This mystery could be solved thanks to research carried out on discrete CP symmetry violation (C stands for charge conjugation and P for parity).

- Why and how do elementary particles have mass? And why is there such a remarkable difference between them (from a few eV to several GeV)? The Higgs mechanism could provide hints to these questions. One of its most noticeable consequences is the prediction of the existence of a scalar neutral particle: the Higgs boson. That particle is till this day the last missing element of the Standard Model.

## 2.3 Top quark physics

The discovery of the top quark in 1995 at Fermilab, by the CDF and D0 experiments located at the proton–proton collider Tevatron further confirmed the hypothesis of the subdivision into 3 families of leptons and quarks as predicted by the Standard Model and opened a new field of research: top quark physics.

Following the Standard Model's elementary particle organization, the top quark is b quark's partner, but it is 35 times heavier. Actually its mass is $171.4\pm2.1$ GeV/$c^2$[?] which represents the most striking of its properties, in fact it is the heaviest known particle.

The study of the top quark has several motivations: within the Standard Model the top quark and the $W$ boson masses provide constraints to the Higgs boson mass; experimentally speaking, the top quark has optimal characteristics for detector calibration; its remarkable properties might shed hints ofphysics beyond the Standard Model.

### 2.3.1 Top quark production in colliders

At $p$–$p$ colliders, top quarks can be produced via : Single top quark production, through the weak force or Top–antitop pair production, through the strong force.

In hadronic[3] colliders such as the LHC the dominant production mode of the top quark is through the strong interaction compared to the – not yet observed – electroweak production. Via the strong interaction which conserves the flavor, the top quark can be produced only with its antiparticle. The gluon–gluon fusion process $gg \rightarrow t\bar{t}$ accounts for about 90% of the total $t\bar{t}$ production, while $q\bar{q} \rightarrow t\bar{t}$ accounts for the rest (*cf.* figure 1).

---

[2]3 gauge couplings, 2 Higgs parameters, 9 quark and lepton masses and charges, 3 mixing angles and a CP violation phase

[3]the term hadron refers to any subatomic particle which interacts via the strong force, *e.g.* a proton is a hadron

The Standard Model prediction[4] for the cross section of $t\bar{t}$ production is $\sigma(t\bar{t}) = 833$ pb, implying the production of over 8 millions $t\bar{t}$ pairs in one year.
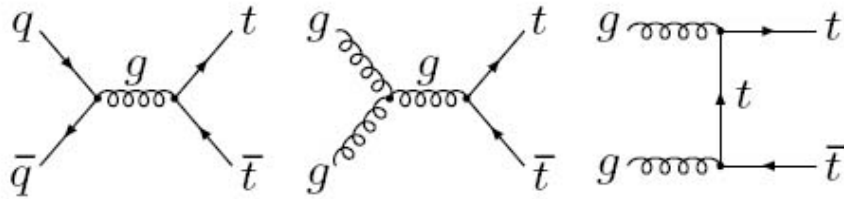


Figure 1: $t\bar{t}$ production via strong interactions, quark–antiquark (left), gluon–gluon fusion (center and right)

The electroweak production of single top quarks has not yet been observed. Still cross section predictions are around 250 pb, implying that this production mode could be not negligible.

### 2.3.2 Characteristics of $t\bar{t}$ events

Figure 2 shows the simulation of a $t\bar{t}$ event inside the ATLAS detector. Within the internal part (tracking system) of the detector one can see a great number of tracks. Inside the electromagnetic (hatched internal part) and hadronic (hatched external part) calorimeters one can see the propagation of two jets.
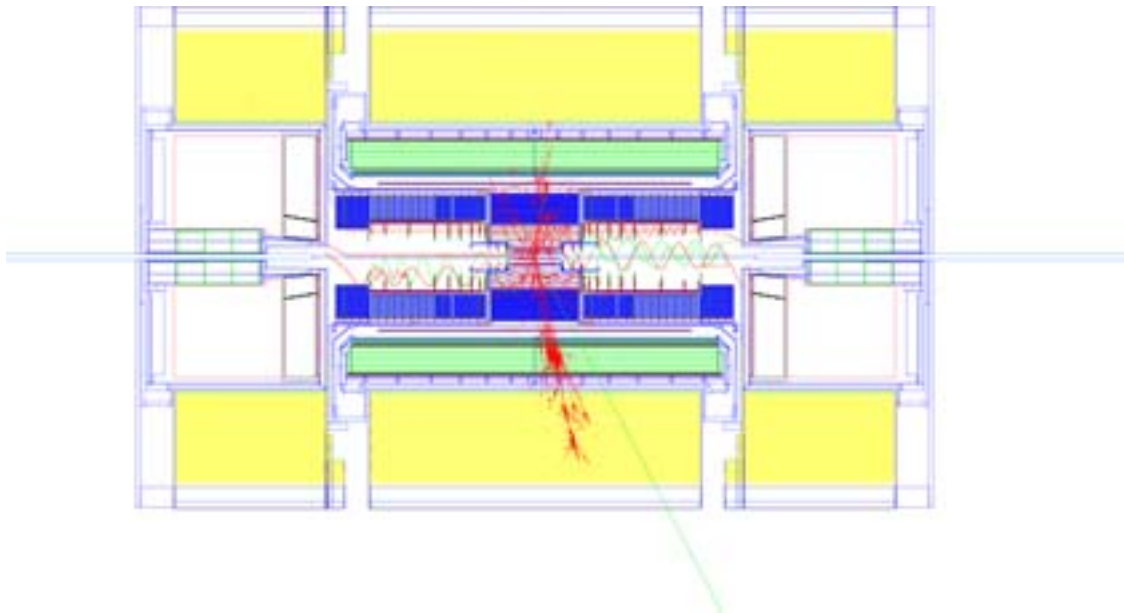


Figure 2: $t\bar{t}$ event simulation inside the inner detector and the calorimeter.

Because of its high mass, the top quark has a very short lifetime. Therefore it will decay to an intermediate state where some of the particles will initiate jets through hadroniza-

---

[4]at the Next to Leading Order level

tion[5]. Consequently, only the top quark decay products will be observed.

There exist three possible top quark decays, however one dominates : the decay $t \rightarrow Wb$ has a probability to occur of 99.8% (*cf.* figure 3). The production channel chosen is
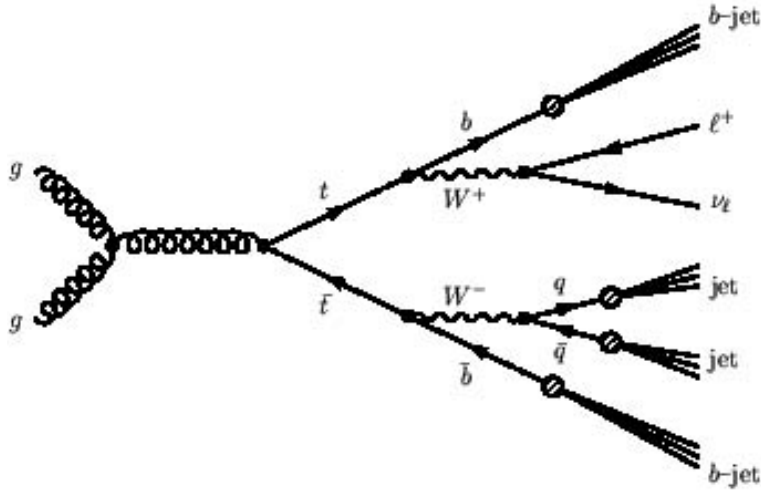


Figure 3: Feynman diagram of the preferred detection channel for the $t\bar{t}$ pairs in ATLAS, with the final state jets and leptons

$t\bar{t}$, so $W^+$ and $W^-$ bosons and 2 b quarks are produced. These last ones hadronize and become jets.

$t\bar{t}$ events can be classified by the decay modes of the two $W$'s. In 1/3 of the cases the $W$ boson decays into a pair of leptons (a charged lepton and its corresponding neutrino) and the rest of the time in a pair $q\bar{q}$ which becomes two jets. As far as the decay of the $W$'s is concerned, there are three main channels of decays, namely:

**Hadronic channel :** It represents 44% of all $t\bar{t}$ events. Both $W$'s decay into quark pairs, which evolve into jets (jets proceeding from the $W$ decay are usually called light jets). The same happens to the remaining $b$ quarks (*cf.* figure 4).

$$t\bar{t} \rightarrow b\bar{b}W^+W^- \rightarrow jjjjjj$$

This channel is heavily affected by background[6] processes due to multi–jets QCD events. Thus an unambiguous identification of the $W$ boson is usually very difficult, due to the many traces left by jets in the calorimeters.

**Semileptonic channel :** This channel represents $\simeq 30\%$ of all $t\bar{t}$ events without taking into account the decay of $W$'s into $\tau$'s. One of the $W$'s decays into a quark pair which evolves into two light jets and the other one decays into 2 leptons (*cf.* figure 4).

$$t\bar{t} \rightarrow b\bar{b}W^+W^- \rightarrow jjjj\ell\nu_\ell$$

---

[5]Hadronization is the process of formation of hadrons out of quarks and gluons, due to quark confinement. A jet is formed and regroups in a narrow cone hadrons and other particles produced by this hadronization.

[6]Physical background is a process which has the same decay products

Since each $W$ decays differently, a distinction between the two top produced can be made: the hadronic side, in which the $W$ decays into 2 light jets, and the leptonic part, in which the other $W$ decays into a charged lepton and its corresponding neutrino.

The presence of an isolated charged lepton with high transverse energy ($E_T$), the missing energy due to the neutrino, four jets among which two are originating from a $b$–quark represent the signature of this channel. The leptonic side, thanks to the presence of the charged lepton allows an "easy" triggering. The presence of the neutrino in the decay products will cause a large missing transverse energy. Therefore the mass reconstruction is difficult in this side. The hadronic side allows an easier mass reconstruction. In the absence of $b$–tagging the largest irreducible contribution to the background originates from $W + 4$ jets events, where the $W$ boson decays leptonically and produces the isolated lepton and missing $E_T$, while the 4 jets can be of any kind. Consequently by finding at least 2 light jets and 2 $b$ jets per event, a satisfactory discrimination between signal and background can be done.

**Dileptonic channel :**  It accounts for $\simeq 5\%$ of all $t\bar{t}$ events without taking into account the $\tau$'s. Each $W$ decays into two leptons. The decays products of the pair $t\bar{t}$ are :

$$t\bar{t} \to b\bar{b}W^+W^- \to e\nu_e e\nu_e + jj$$

$$t\bar{t} \to b\bar{b}W^+W^- \to e\nu_e \mu\nu_\mu + jj$$

$$t\bar{t} \to b\bar{b}W^+W^- \to \mu\nu_\mu \mu\nu_\mu + jj$$

The di–leptons channel is interesting because it has a very clear signature and a reduced physical background (*cf.* figure 4). The presence in the final state of two leptons reduces the instrumental background, because for a multijet event to simulate a dilepton $t\bar{t}$ event it is required that two jets be identified as leptons, which is very unlikely. The presence of large missing transverse energy – due to the two neutrinos in the final state – will make the top quark mass measurement challenging in this channel.
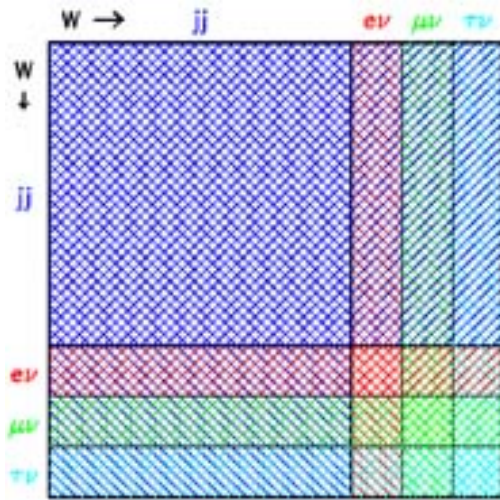


Figure 4: Top quark decay channels

### 2.3.3 Reducible backgrounds

A much harder to evaluate and completely different type of background is the reducible background, originating from non–perfect detector performance. For example, sometimes $\pi$ and $K$ particles can be wrongly identified in the detector as leptons. Due to fluctuations in the jet fragmentation process and in the detector response, we can get events which seem to contain a high $p_T$ isolated lepton and missing energy, but do not. The probability that this happens in any given event is very low, but the jet production cross section is much larger than the $W$ production cross section. In addition, there will be electrons from non–identified photon conversions and leptons from beauty decays which are wrongly taken as coming from a $W$ decay. The QCD multijet background cannot be realistically generated through a Monte Carlo. Its effect depends crucially on the capability of the ATLAS experiment to minimize the misidentification and increase the electron/pion separation.

# 3 The ATLAS experiment

The acronym ATLAS (**A T**oroidal **LHC A**pparatus **S**ystem) not only designates a detector but also a physics experiment shared by a worldwide collaboration of over 1800 physicists and engineers from 150 laboratories from 34 different countries who have embarked in this scientific adventure.

The detector is one of the largest and most complex ever built in particle physics for a variety of reasons. For instance, for its construction, new state–of–the–art radiation–resistant electronics were developed as well as computing frameworks to handle the immense output of data but also important innovations in the fields of mechanical and civil engineering, cryogenics and geodesy were made.

## 3.1 The LHC at CERN

Th LHC (Large Hadron Collider), it is the largest particle accelerator ever conceived and it is currently under construction at CERN[7](European Laboratory for Particle Physics) near Geneva, the world's largest particle physics laboratory. Collisions at the LHC will start in 2007 and continue to happen for at least 10 more years. Proton–Proton Collisions as well as Pb–Pb nuclei collisions will take place at the LHC.

CERN's network of previous accelerators allows production and pre–acceleration of particles before their injection into the LHC. In the case of protons, they are initially accelerated by a linear accelerator up to 50 MeV, then by 3 successive circular accelerators, the Booster up to 1 GeV, the PS (Proton Synchrotron) up to 26 GeV and finally the SPS (Super Proton Synchrotron) up to 450 GeV. The protons are later injected into the main LHC ring and accelerated up to 7 TeV. This results into an energy in the center of mass of the collision of 14 TeV. The underground tunnel where the LHC is being built used to belong to CERN's previous accelerator, called LEP (Large Electron Positron Collider). In this way CERN reuses its existing infrastructure, save a few modifications, thus lowering costs. The tunnel has a perimeter of 26.7 km. Protons will be assembled in bunches. Inside the LHC there will be 2835 bunches per ring (There are 2 rings, in which protons are accelerated equally but in opposite directions) spaced at a distance of 7.48 m which corresponds to a time interval of 24.95 ns. Each of these bunches will

---

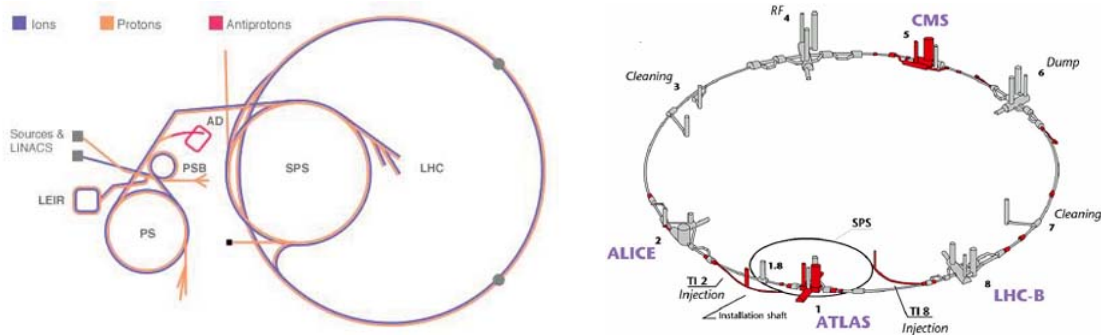[7]originally from French : Conseil Européen pour la Recherche Nucléaire

Figure 5: CERN's accelerator network

contain $1.05 \times 10^{11}$ protons. This time interval between bunches gives us a mesure of the collision rate expected at the LHC.

To curve the particle beams, a series of superconducting magnets were developed. These are composed of a magnetic cylinder head and a cryogenic infrastructure, which keeps the head at a temperature of 1.9 K by using super–fluid liquid helium. The head produces a magnetic field of 8.4 T within the two beam pipes. To obtain the desired collisions the beams will cross at 4 points. These 4 points also represent the location of the detectors that will measure the products of such collisions. These 4 detectors are: ATLAS, CMS, LHCb and ALICE.

ATLAS and CMS are general purpose detectors, while LHCb was created for the study of $b$–quark physics and ALICE for the study of quark–gluon plasma physics by colliding heavy ions, mainly lead nuclei.

## 3.2 The ATLAS detector

ATLAS is one of two general purpose detectors at LHC. It is located at point 1 (*cf.* figure 5), on the rear of CERN's main entrance. The ATLAS detector consists of four major components, the Inner Tracker which measures the momentum of each charged particle, the Calorimeter which measures the energies carried by the particles, the Muon spectrometer which identifies and measures muons and the Magnet system that bends charged particles for momentum measurement. The detector is a cylinder with a total length of 42 m and a radius of 11 m and weighs approximately 7000 t (*cf.* figure 6).

### 3.2.1 Coordinate system

The beam direction defines the $z$–axis, and the $x$–$y$ plane is the plane transverse to the beam. The positive $x$–axis is defined as pointing from the interaction point to the center of the LHC ring, and the positive $y$–axis is pointing upwards. The azimuthal angle $\phi$ is measured around the beam axis, and the polar angle $\theta$ is the angle from the beam axis (*cf.* figure 7).

However, instead of using the normal polar angle $\theta$, an angular quantity called *pseudo-rapidity* is employed, designated by the letter $\eta$ and which is related to $\theta$ by the following equation :

$$\eta = -ln\left(tan\left(\frac{\theta}{2}\right)\right)$$

It is a handy variable to approximate the *rapidity* if the mass and momentum of the
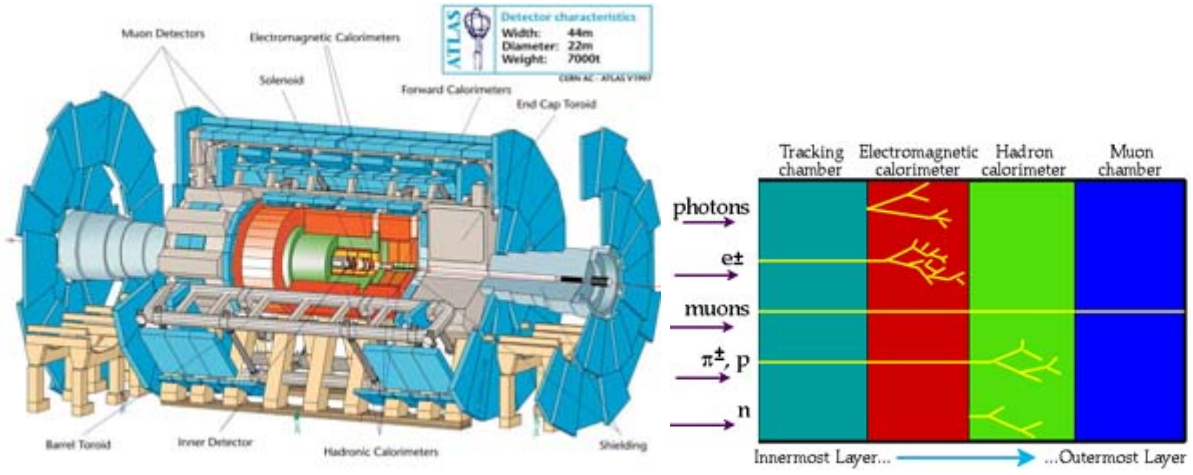
Figure 6: On the left the ATLAS detector and on the right a chart of the particle detecting capabilities of each subdetector
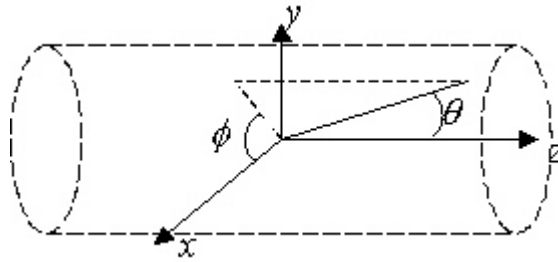


Figure 7: ATLAS' coordinate system

particle are not known. $\eta$ is the same as the rapidity $y$ if one sets $\beta = \frac{v}{c} \to 1$ or $m = 0$.

The rapidity $y$ is defined by :

$$y = \frac{1}{2} ln \left( \frac{E + p_L}{E - p_L} \right)$$

Where $p_L$ is the longitudinal momentum and $E$ is the energy of the incident particle. It turns out rapidity differences are invariant under lorentz boosts but also statistical particle distributions are flat in $y$ for many physics production models.

Nevertheless statistical distributions plotted in $\eta$ rather than $y$ undergo transformations that have to be estimated by using a kinematic model for the interaction.

**Luminosity**   :

It relates the cross–section $\sigma$ of a given process to the corresponding event rate $R$ :

$$R = L \times \sigma$$

Therefore, luminosity $L$ is by definition a process–independent quantity which is completely determined by the properties of colliding beams. It can be thought of as the amount of particles colliding per unit area per unit time and it is an important value to characterize the performance of an accelerator.
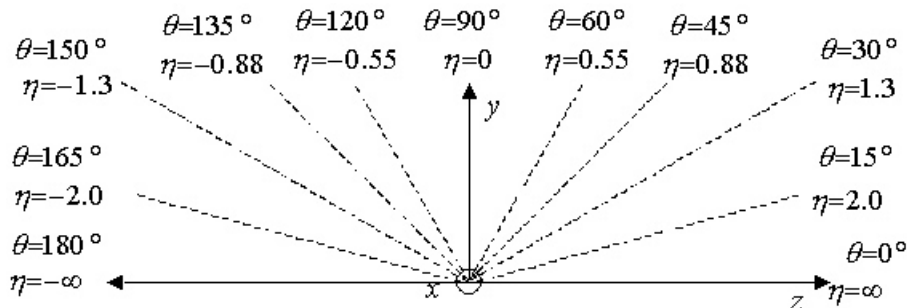
Figure 8: Corresponding values of $\eta$ for different values of $\theta$

It can be roughly estimated by using the following equation :

$$L = nf\frac{N_1 N_2}{A}$$

where $n$ is the number of bunches of particles in each beam (typically 4–8), $f$ is the revolution frequency ($f = 11$ kHz for the LHC), $N_1$ and $N_2$ are the number of particles in each bunch and $A$ is the area of each beam.

The LHC will attain a luminosity of $10^{33}$ cm$^{-2}$ s$^{-1}$ shortly after its start–up (Regarded as the low luminosity period), but will eventually reach its full luminosity of $10^{34}$ cm$^{-2}$ s$^{-1}$.

### 3.2.2 Tracking system or Inner Detector

It begins just after the beam pipe and extends to a radius of 1.2 m and is 7 m long. Its purpose is to track charged particles by detecting their interaction with material at discrete points, revealing crucial information about the particle's type, charge and momentum. A magnetic field surrounding the inner detector causes charged particles to curve; the direction of the curve reveals the particle's charge while the radius of curvature its momentum given by the well–known expression $p = qBr$, where $p$ is the magnitude of the momentum, $q$ is the electric charge, $B$ the magnitude of the magnetic field and $r$ is the radius of curvature (this holds only when the direction of motion is perpendicular to the direction of the magnetic field). The starting points of the tracks also yield useful information for identifying particles. The inner detector is composed of 3 parts (*cf.* figure 9):

**Pixel detector** :
It is the innermost part of the detector, it contains 3 cylindrical layers in the barrel and 3 disks on each end–cap, with a total of 1744 modules. The considerably small pixel size is intended for extremely precise tracking very close to the interaction point.

Each time a charged particle traverses one of the layers, a signal is produced, thereby giving a measurement of the particle's position precise enough to determine whether the particle originated at the proton–proton collision point or a few millimeters from it as a decay product of another particle. This is better known as vertex.

It is interesting to mention that due to this proximity to the interaction point, the pixel detector is subject to a great deal of radiation, therefore all components had to be radiation hardened in order to continue operating after significant exposures.

**Semi–Conductor Tracker (SCT)** :

It is the middle component of the inner detector. It is similiar in concept and function to the preceding part of the detector. This allows a large covered area for a lower price and a reduced granularity. The SCT is composed of four double layers of silicon strips and is designed to provide eight precision measurements per track in the intermediate radial range, contributing to the measurement of momentum, impact parameter and vertex position. The SCT covers $|\eta| < 2.5$.

**Transition Radiation Tracker (TRT)** :

The outer tracker of ATLAS is a combined straw tube tracker and transition radiation detector. It consists of several tens of thousand radial straws. Each straw is filled with a gas that is ionized whenever charged particles pass through. The ions are then drawn to the inner wall of the straw while the electrons are drawn to a wire maintained at a higher potential (than the inner wall) and this causes the appearance of a current through this wire. This happens within several straws creating a pattern of signals that allow the path of the particle to be determined. The straws also contain materials with different indeces of refraction, causing charged particles to produce transition radiation and leave much stronger signals in each straw. Thus it has a standalone electron identification capability.

The TRT provides on average 36 two–dimensional measurement points with 0.170 mm resolution for charged particle tracks with $|\eta| < 2.5$ and $p_T > 0.5$.
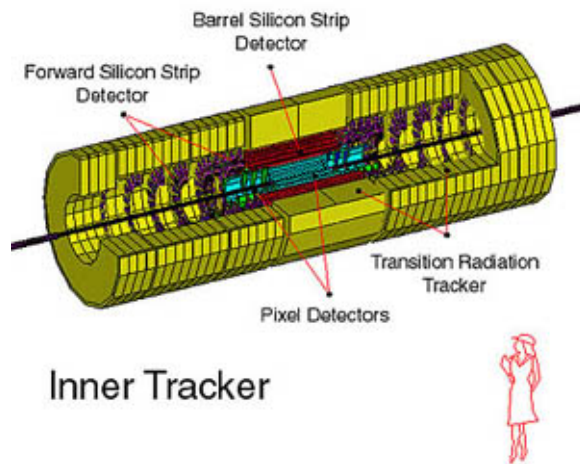


Figure 9: ATLAS' inner detector

### 3.2.3   Calorimetry

There are 2 calorimeters in ATLAS; the electromagnetic calorimeter and the hadronic calorimeter. Both lie outside the solenoidal magnet that surrounds the inner detector. Their purpose is, mainly, to measure the energy from particles by stopping them. This takes place with the development of a shower which is a cascade of secondary less–energetic particles, which in turn produce even more particles with lesser energy and so forth, due to their interaction with dense matter. This process goes on till the particles produced have so little energy that they are absorbed by the material. There are 2 basic types of showers; electromagnetic showers and hadronic showers.

**Electromagnetic calorimeter** :

It is a sampling calorimeter with "accordeon–shaped" lead electrodes (*cf.* figure 10). There are also presamplers consisting of one layer of LAr in front of the electromagnetic calorimeter which help to correct for the energy loss in front of the calorimeter (mainly due to the cryostat walls and the barrel solenoid). Particles which interact electromagnetically deposit most of their energy in this calorimeter. These include photons and charged particles (mostly electrons). The electromagnetic calorimeter is also able to localize to a certain extent the particles that pass through it. Electromagnetic showers in this calorimeter occur within the lead plates (dense material) which are immersed in liquid argon (*cf.* figure 11). Such LAr gaps (about 4 mm) between plates are subject to a large electric field, so when the shower of electrons or positrons traverses them, they ionize the argon. The ionization electrons drift towards the higher potential side (far more quickly than the remaining ions) and their motion produces an electric current in an external circuit connected to the calorimeter. The greater the incident energy of a particle entering the electromagnetic calorimeter, the more shower electrons there will be and thus greater the current.
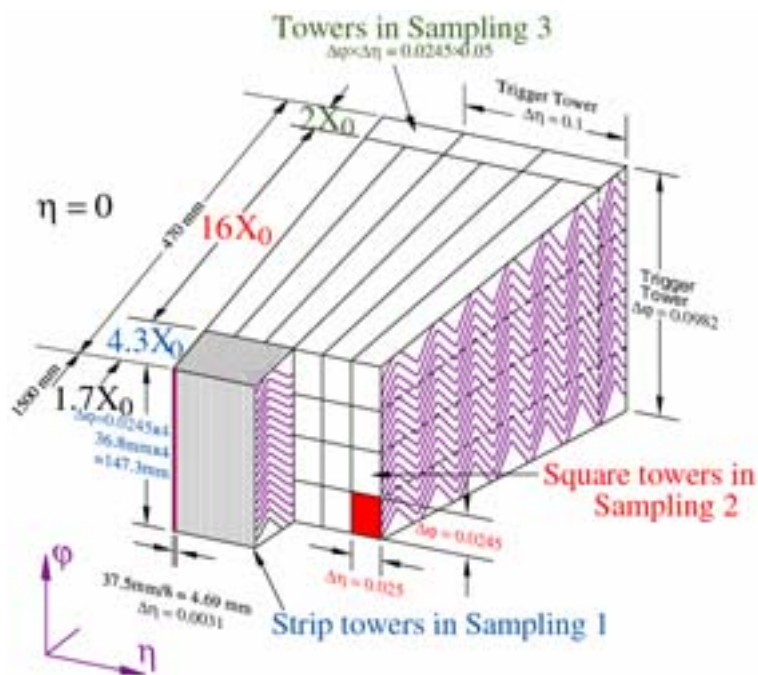


Figure 10: Granularity of the electromagnetic calorimeter

**Hadronic calorimeter** :

It measures energy from particles that go through the electromagnetic calorimeter without interacting much (or not at all). These particles are primarily hadrons (hence the name). The hadronic calorimeter is composed of 2 parts, the tile calorimeter and the liquid argon end cap hadronic calorimeter.

The tile calorimeter is a large sampling calorimeter that makes use of steel as the absorber material and scintillating plates. It covers the central range $|\eta| < 1.7$. The new feature of its design is the orientation of the scintillating tiles which are placed in planes perpendicular to the colliding beams and are staggered in depth. Interactions of high energy hadrons in the plates transform the incident energy into a hadronic shower. This

Figure 11: Simulation of the development of an electromagnetic shower in the electromagnetic calorimeter
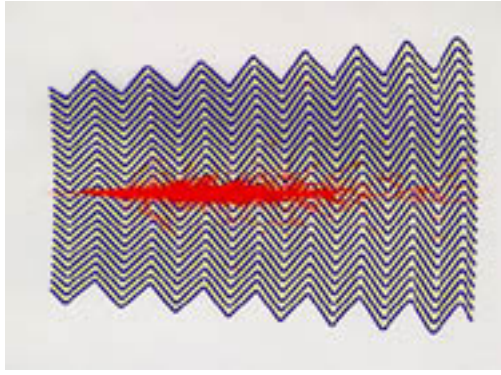
shower, when traversing the scintillating tiles, causes them to emit light in an amount proportional in the incident energy.

The liquid argon end cap hadronic calorimeter is very similar in principle to the electromagnetic calorimeter, except it uses copper plates instead of lead plates which are more appropiate to the hadronic showering process and the argon gaps are twice as large. The total radiation emanating from the collision point is least intense at small values of $\eta$, and most intense at larger values. Because scintillating tiles are damaged by excessive exposure to radiation, hadronic calorimetry in the region $|\eta| > 1.7$ is provided by this device.

### 3.2.4   Muon spectrometer

It is basically an enormous chamber tracker. Its tremendous size is required to accurately measure the momentum of muons, which penetrate other elements of the detector without being stopped; the effort is vital because muons are a key element in a number of interesting physical processes and because the total energy of particles in certain events could not be measured accurately if they were ignored. Muons curve in order for their momentum to be measured, though with a different magnetic field, lower spatial precision and a quite larger volume.

### 3.2.5   Magnet system

**Central Solenoid**  : The central solenoid has a length of 5.3 m with a bore of 2.4 m. The conductor is a composite that consists of a flat superconducting cable located in the center of an aluminum stabilizer with rectangular cross–section. It is designed to provide a field of 2 T in the central tracking volume with a peak magnetic field of 2.6 T. To reduce the material build–up the solenoid shares the cryostat with the liquid argon calorimeter.

**Toroid Magnet**  : The ATLAS Toroid Magnet system consists of eight barrel coils housed in separate cryostats and two end–cap cryostats housing eight coils each. The end–cap coils systems are rotated by 22.5º with respect to the barrel toroid in order to provide radial overlap and to optimize the bending power in the interface regions of both coil systems. The magnetic field produced by the toroid is not uniform, but measurements need to be much less precise to measure momentum accurately in the large volume of the muon system.

### 3.2.6   Trigger system

It is essentially a primary filter of events. The task of the trigger is to select interesting physics events in an efficient and controlled way and to write the data produced by the ATLAS detector for these events to permanent storage for later analysis. The event rate must be lowered by a factor $10^7$ through the use of the trigger system, simply because this is the event rate at which data can be written to permanent storage.

To achieve this filtering very inclusive triggers can be carried out at early selection stages, for example selections of events containing high–$p_T$ muons, photons, electrons, taus, hadrons and jets as well as events with very large missing transverse energy or total scalar transverse energy. At later selection stages inclusive selections can be made of leptonic $W$ and $Z$ decays, making use of invariant mass information in the case of $Z$ decays and missing transverse energy in the case of $W$ decays.

The trigger system is organized in 3 levels:

**Level 1 (LVL1)**   : It receives data from the LHC at the bunch–crossing rate of 40 MHz and provides a selection decision for each bunch crossing every 2 $\mu$s, therefore information is temporary stored in pipeline memories during this period. The selection is carried out by special purpose processors (solely hardware based selection) which roughly identify, for each event, regions of the detector containing interesting features such as high–$p_T$ electromagnetic clusters, jets and muons. The LVL1 trigger is able to lower the data acquisition rate to 100 kHz.

**Level 2 (LVL2)**   : The task of the LVL2 trigger is to reduce the acceptance rate to $\sim 1$ kHz. The LVL2 trigger has to process the data labeled by the LVL1 trigger as containing interesting information. The LVL2 uses full–precision information from the inner tracking detector, as well as from the calorimeters and muon spectrometer (dedicated algorithms are applied and optimized for the speed of processing). The average decision time for the LVL2 trigger is close to 10 ms, thus the data sent by the LVL1 to the LVL2 is queued up in a buffer.

**Event Filter (EF)**   : After an event is accepted by the LVL2 trigger, all the data for that event is sent to the Event Filter (EF). Complete event reconstruction is possible at this third stage of triggering. The average decision time for the EF is estimated to be $\sim 1$ s. The EF must lower the event rate to 100 Hz and perform a data–storage rate of the order of 100 MB/s.

In order to achieve this, full event data is used together with the latest available calibration and alignment information. This is the final selection before the recording of events for offline analysis.

## 3.3   Data flow

The ATLAS data taking will start in 2007. To prepare the physics analysis a scheme of simulated data production is used. It is similar to the one which will be used for real data.

Figure 12 shows a simplified view of the processing stages in the simulation data flow. Input for simulation comes from event generators. Data objects representing Monte Carlo truth information from the generators are read by simulation and processed. Hits produced by the simulation can be directly processed by the digitization algorithm and then

reconstructed. The stages in the simulation data–flow pipeline are described in more detail
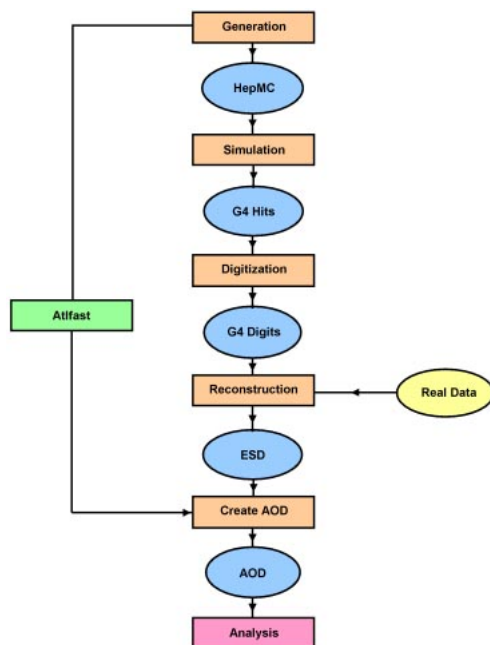


Figure 12: Simulation data flow stages

in the following. In addition to the full simulation framework, ATLAS has implemented a fast simulation framework that substantially reduces the processing requirements in order to allow larger samples of events to be processed rapidly, albeit with reduced precision (called ATLFAST). Only the full simulation framework is described below.

### 3.3.1 Physics generation

Event generators are indispensable as tools for the modeling of the complex physics processes that lead to the production of hundreds of particles per event at LHC energies. Generators are used to set detector requirements, to formulate analysis strategies, or to calculate acceptance corrections. They also illustrate uncertainties in the physics modeling.

Generators model the physics of hard processes, initial and final–state radiation, multiple interactions and beam remnants, hadronization and decays, and how these pieces come together. These generators are based on the Monte Carlo technique (*e.g.* PYTHIA and HERWIG).

The individual generators are run from inside ATHENA (ATLAS offline software framework) and their output is converted into a common format by mapping into HepMC (Monte Carlo Generator 4–Vector Classes). The event is presented for downstream use by simulation, for example by G4ATLAS simulation (using GEANT4) or the ATLFAST simulation.

### 3.3.2 Detector response simulation

The ATLAS detector simulation is now based on GEANT4, a toolkit which provides both a framework and the necessary functionality for running detector simulation in particle physics and other applications. The functionalities provided include optimized solutions

for geometry description and navigation through the geometry, the propagation of particles through detectors, the description of materials, the modeling of physics processes.

**Pile–up** :
G4ATLAS produces hits as output, which are a record of the real interactions of particles in the detector. At higher machine luminosities, however, multiple interactions can occur at each beam crossing (typically one signal event with multiple minimum–bias background events), and in addition other backgrounds (*e.g.* cavern background) need to be taken into account. Pile–up (*i.e.* the overlaying of signal and background events) is an optional processing stage in the simulation processing pipeline.
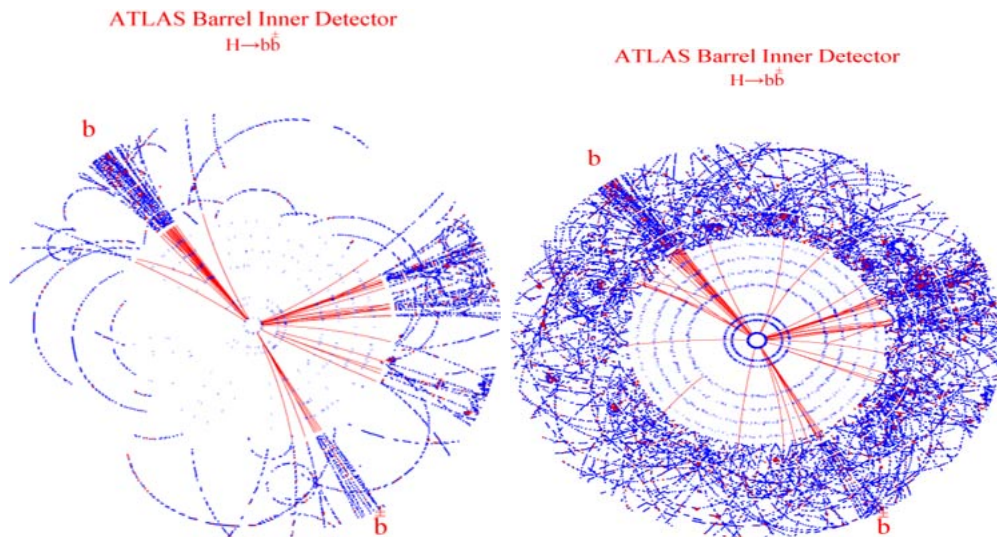


Figure 13: Simulation of an event $H \rightarrow b\bar{b}$ inside the inner detector at low luminosity (left) and high luminosity (right)

Figure 13 shows a simulation of Higgs boson decaying into a pair of $b\bar{b}$. The two quarks hadronize into jets. On the left the pile–up of 2.4 events is added corresponding to the low luminosity period while on the right, 23 events are added corresponding to the high luminosity period. The reconstruction and identification of jets are much harder in the second case.

**Digitization** :
The hits produced either directly by G4ATLAS, or from the merging of pile–up events, need to be translated into the output actually produced by the ATLAS detectors. The propagation of charges (as in the tracking detectors and the liquid argon calorimeter) or light (as in the case of tile calorimeter) into the active media has to be considered as well as the response of the readout electronics. The final output of the digitization step are Raw Data Objects (RDO's) that should resemble the real detector data.

### 3.3.3   Event selection and reconstruction

The ATLAS detector will produce approximately 3 PB (PetaByte) of raw data per year. A vast amount of information which prohibits the simple distribution to worldwide collaborators. To enable physicists to analyze the data at remote sites, several different types

of datasets, corresponding to different stages of reconstruction, are produced. Thus the following datasets are available:

* Raw Data Object (RDO). As said before these objects are similar to real detector data.

* Event Summary Data (ESD) which contains the detailed output of the detector reconstruction and is produced from the raw data. It contains sufficient information to allow particle identification, track re–fitting, jet calibration etc. thus allowing for the rapid tuning of reconstruction algorithms and calibrations.

* Combined Ntuple (CBNT), similar to ESD but with less information. Directly usable by ROOT, the analysis and histogram visualization package used in particle physics.

* Analysis Object Data (AOD) which is a summary of the reconstructed event, and contains sufficient information for common analyses. The AOD can be produced from the ESD.

The reconstruction processing pipeline can be decomposed into several stages. The Primary stages are:

* Detector and combined reconstruction (henceforth "Reconstruction"): This includes the reconstruction of the tracking, calorimetry and muon detectors, $i.e.$ jet reconstruction or electron, $\gamma$ and $\mu$ identification. The output is stored and defines the content of the ESD. It contains tracks in the inner detector or the muon spectrometer. Electromagnetic and hadronic clusters are built. These objects contain variables describing the characteristics of the particles ($e.g.$ electromagnetic shower shape variables), but no identification selection is applied. Also some complex algorithms are applied, like the tagging of the flavor of jets ($i.e.$ $b$, $c$ or light jets).

* Analysis preparation. This step includes the reconstruction of complex objects like electrons, $\gamma$'s, $\mu$'s and jets, and reduces the information to an acceptable size for wide distribution. The output defines the AOD content.

The role of reconstruction is to derive from the stored raw data the relatively few particle parameters and auxiliary information necessary for physics analysis: $\gamma$'s, electrons, $\mu$'s, $\tau$'s, $K_0$'s, jets, missing transverse energy, primary vertex. Information from all detectors is combined so that the four–momentum reconstruction is optimal for the full momentum range, full rapidity range and any luminosity, and so that particles are identified with the least background, with the understanding that the optimum between efficiency and background rejection can be analysis–dependent.

## 3.4   Data sample

The CSC layout is used. Data used in the performance evaluation was produced after the CSC data challenge. Release 11.0.42 was used for generation, simulation and reconstruction.

Two data types are used in the following:

To evaluate the performance of the identification algorithm, single electrons samples with pseudorapidity $|\eta| < 2.5$ and $p_T = 20$ GeV and $p_T = 60$ GeV are used. Events with $Z$ decays ($Z \rightarrow e^+ e^-$ and $Z \rightarrow \mu^+ \mu^-$) are also used for lepton identification as well as

some missing transverse energy ($E_T^{miss}$) studies. To evaluate the rejection factors QCD dijet events, including initial and final state radiation, are used. On parton level each jet is required to have a transverse momentum $p_T \geq 17$ GeV/c and a rapidity within $\pm 2.7$. Detailed information about the samples is given in table 2.

| Data | $p_T$ [GeV] | dataset | number of events |
|---|---|---|---|
| single electrons | $= 20$ | 007002 | 48000 |
| single electrons | $= 60$ | 007005 | 45300 |
| dijets | $\geq 17$ | 005802 | 86000 |
| $Z \to e^+e^-$ | | 005144 | 499650 |
| $Z \to \mu^+\mu^-$ | | 005145 | 54000 |

Table 2: Data samples used for performance tests

For the top quark analyses two data samples are used. One containing signal events $t\bar{t}$ and the other is a W + 4 jets[8] sample which represents the most important background source of the semileptonic channel which is to be studied. Detailed information about both samples is given in table 3.

| Data | dataset | number of events |
|---|---|---|
| T1 | 005200 | 201050 |
| W + 4 jets | 003017 | 110000 |

Table 3: Data samples used for top quark analysis

---

[8]this sample corresponds to the Rome layout and the reconstruction release 10.0.1

# 4 Particle identification

Particle identification is the process of using information left by an elementary particle passing through a particle detector to identify the type of particle. The algorithms – and their performance – used in ATLAS for jet and electron reconstruction are described.

Missing energy refers to energy which is not detected in a particle detector, but is expected because of conservation of energy and conservation of momentum. For example, if an electron and a positron collide head–on at equal speeds in the lab frame, any net momentum of outgoing particles indicates missing energy in the opposite direction. Missing energy is generally attributed to particles which escape the detector without being detected, although apparent missing energy may be caused by mismeasurement of the energy/momentum of detected particles. In such events as $t\bar{t}$ where an undetected neutrino is present in the final state, some missing energy will be present.

## 4.1 Jet reconstruction

At hadron colliders, the most prominent signature for a hard scattering to take place is the production of particles with a large total transverse momentum, *i.e.* the jets.

### 4.1.1 Algorithm

Jets are reconstructed by the classical "cone" algorithm which builds a jet around a seed which is representative of the core of the jet and identified usually as the tower (*i.e.* pre–cluster) with highest transverse energy[**?**]. A cone size $\Delta R = 0.4$ is used in the following.

### 4.1.2 Jet definition

Jets objects can be separated into three categories described below: purely electromagnetic jets (rejected as jet candidates in our analysis),$b$–jets and light jets.

**Purely electromagnetic jets** :
Electromagnetic particles $(e^+, e^-, \gamma)$ are usually also reconstructed as jet objects. Figure 14 (top–left) shows the distribution of the distance $(\Delta R = \sqrt{\Delta\phi^2 + \Delta\eta^2})$ between a given jet and the closest electromagnetic cluster versus the ratio between the cluster energy and the jet energy. A jet is labeled electromagnetic if this distance is below 0.2, and the energy ratio above 0.8. Other variables have been studied and we have obtained similar results.
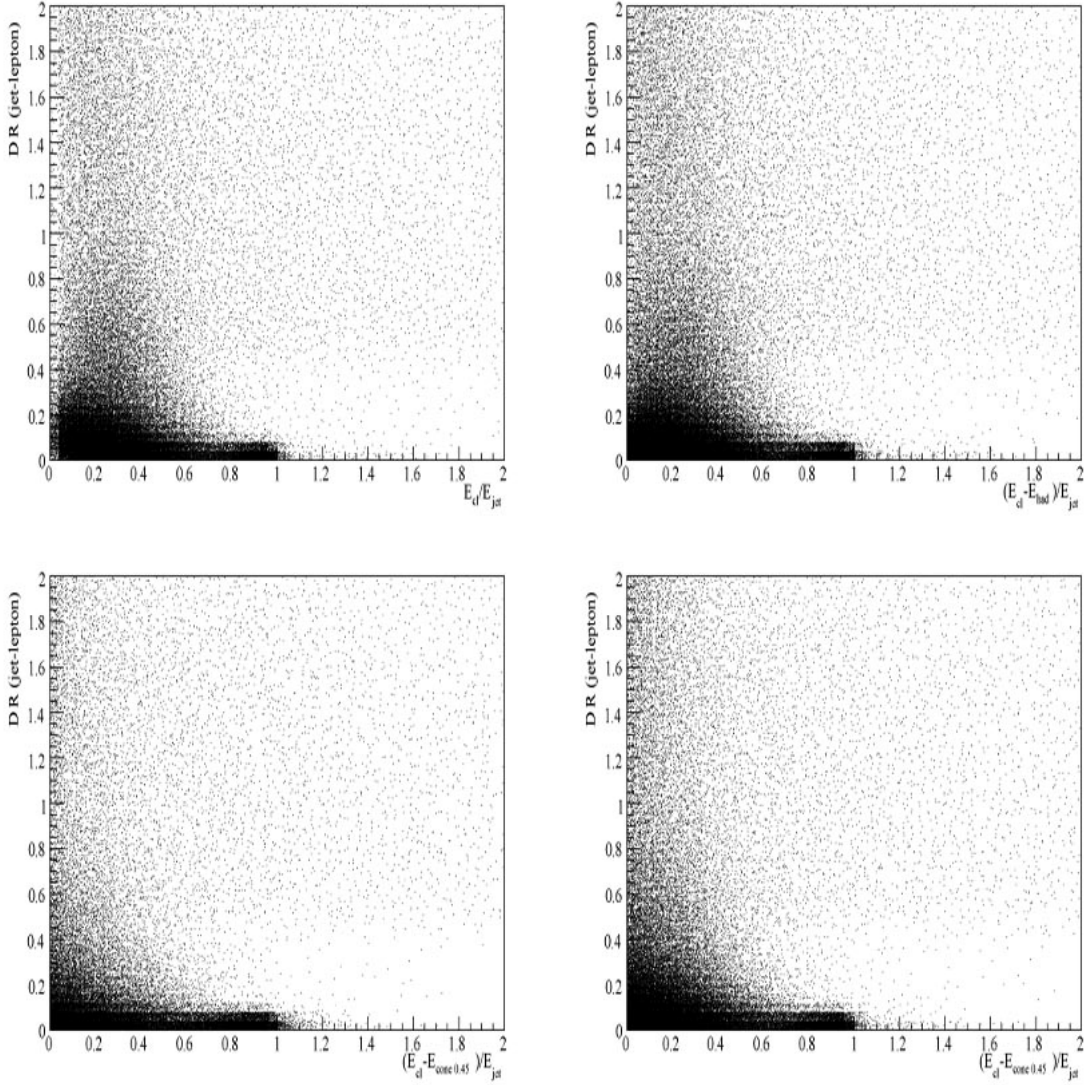
Figure 14: Distance $\Delta R$ between a jet and the closest electromagnetic cluster as a function of the ratio $E(\mathrm{cl})/E(\mathrm{jet})$ (top left), $(E(\mathrm{cl}) - E(\mathrm{had}))/E(\mathrm{jet})$ (top right), $(E(\mathrm{cone}0.2) - E(em, 3 \times 7)/E(\mathrm{jet})$ (bottom left), $(E(\mathrm{cone}0.4) - E(em, 3 \times 7)/E(\mathrm{jet})$ (bottom right).

Figure 15 shows the distribution of the number of jets per event for all events and for the signal sample.
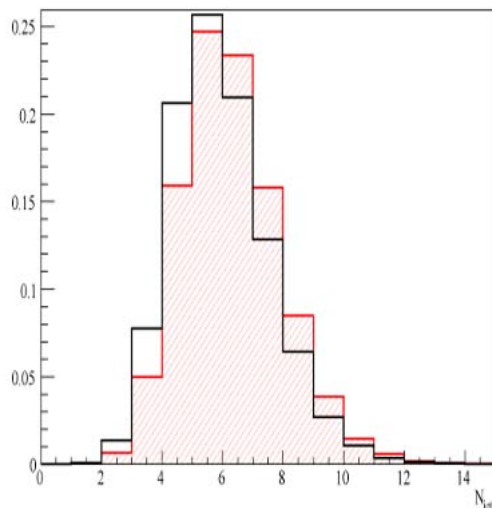


Figure 15: Number of jets with $p_T > 20$ GeV/c and $|\eta| < 2.5$ for all events (empty histogram) and for top events (shaded histogram).

Figure 16 shows the distribution of $p_T$ and $\eta$ for the selected jets.
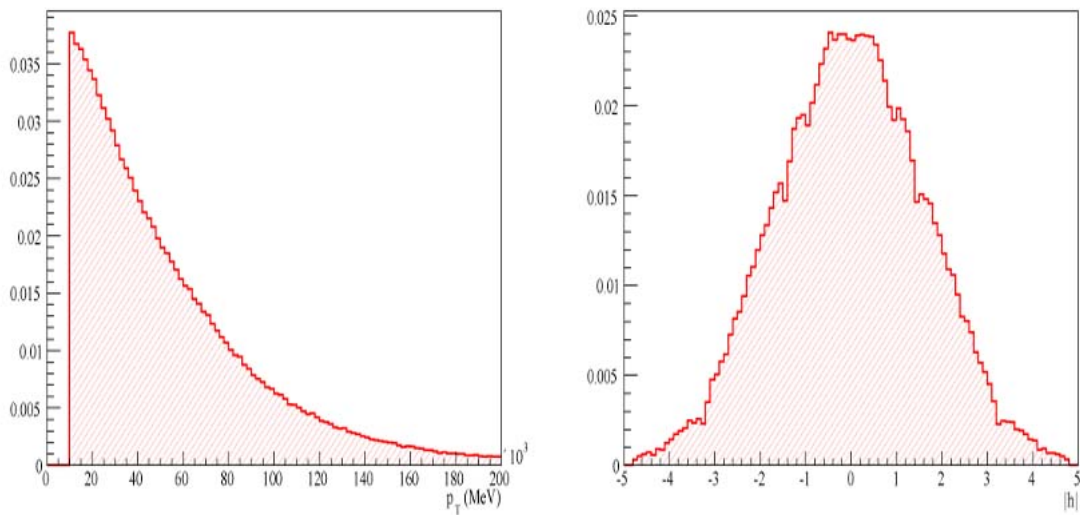


Figure 16: Distribution of $p_T$ (left panel) and $\eta$ (right panel) for the selected jets for signal sample (shaded histogram) and for background sample (empty histogram).

$b$–**jets** :

The $b$–tagging algorithms are implemented in ATHENA but are available only at the AOD level. Since our analysis is done at CBNT level (*i.e.* before AOD creation) it is not possible to use them. Therefore, a hand–made $b$–jet definition is used based on the

distribution of figure 17 of the distance between a true $b$–quark, coming from the decay of the corresponding top, and the closest non–electromagnetic jet. The jet is tagged as a $b$–jet if this distance is smaller than 0.2. The efficiency of this tagging is equal to 90%, thus much higher than a realistic $b$–tagging ($\sim$60%).
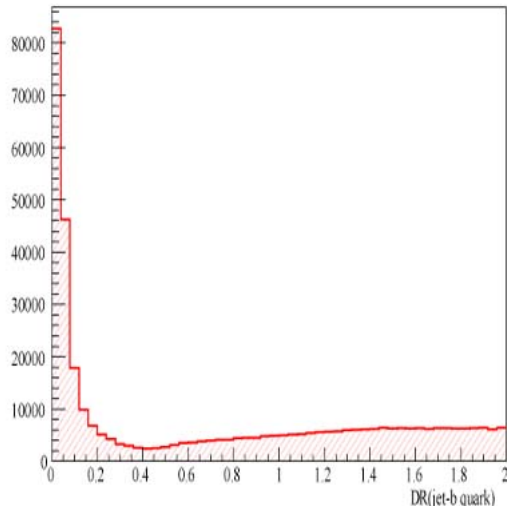


Figure 17: Distance $\Delta R$ between a $b$–quark and the closest non–electromagnetic jet.

**light jets** :
The remaining jets, which are not purely electromagnetic jets and not $b$–tagged, are called light jets.

### 4.1.3 Jet energy precalibration

As explained in the next section, the event selection begins with a preselection which consists in applying several cuts and among them, cuts on the jets transverse energy. Therefore, a precalibration of this energy needs to be performed at the first level of our analysis, for $b$–jets and light jets. This calibration relies on the Monte Carlo information for both jets. We study the ratio of the jet energy reconstructed over the corresponding true quark for $b$–jets, and the corresponding Monte Carlo jet, as a a function of energy, in bins of $\eta$[9].

**Light jets energy precalibration** :
Figure 18 (left panel) shows the ratio between the reconstructed energy of the light jet over the corresponding Monte Carlo jet energy[10] as a function of the Monte Carlo jet energy, for the five studied ranges in $\eta$. The calibration factors, function of energy and defined for each range in $\eta$ are given by the mean value of the profile histogram. Figure 18 (right panel) shows the same variable, after calibration, integrating over all $\eta$ values: the residual

---

[9]The $\eta$ regions [0;2.5] has been divided into five ranges for this study: $|\eta| \leq 0.6$, $0.6 < |\eta| \leq 1$, $1 < |\eta| \leq 1,4$, $1.4 < |\eta| \leq 1.8$, $1.8 < |\eta| \leq 2.5$. These ranges correspond to calorimetric regions where the behavior is roughly constant

[10]Among the Monte Carlo jets, the one associated to a reconstructed jet is the closest one, provided the distance between the Monte Carlo jet and the jet is smaller than 0.2.

miscalibration is smaller then 1 GeV, except at very low energy, which is satisfactory given the value of the jet transverse momentum cut applied later ($> 20$ GeV).
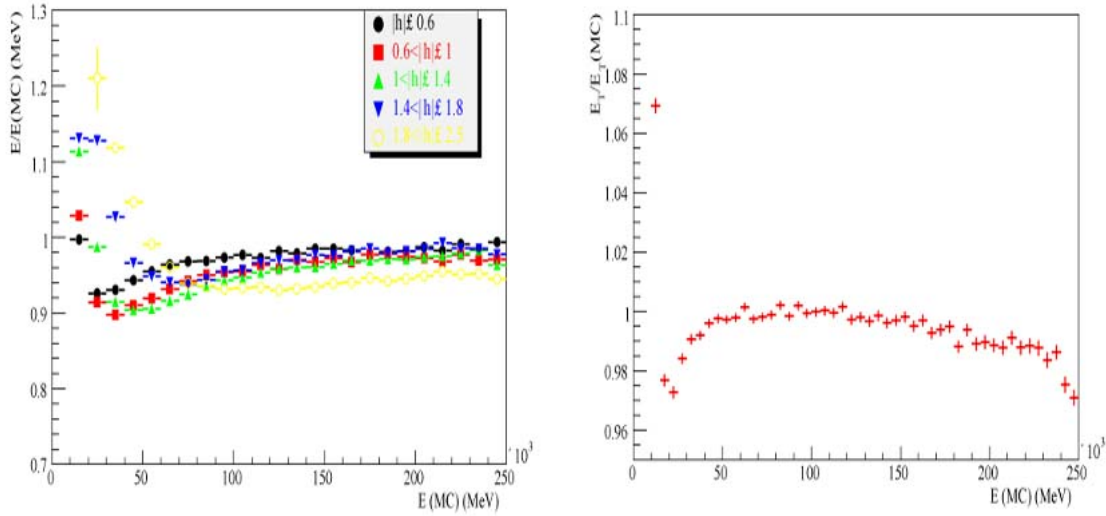


Figure 18: Left: ratio between the reconstructed light jet energy and the corresponding Monte Carlo jet energy, as a function of the Monte Carlo jet energy and for different ranges in $\eta$. Right: check of the light jet energy calibration.

**light jets energy resolution** :
Energy resolution follows from the calibration study described above: the distribution of the difference between the light jet energy and the corresponding Monte Carlo jet energy has been studied for several energy bins, and fitted by a gaussian whose width corresponds to the energy resolution. Figure 19 shows the behavior of this resolution, as a function of the energy of the light jet, for different $\eta$ ranges.
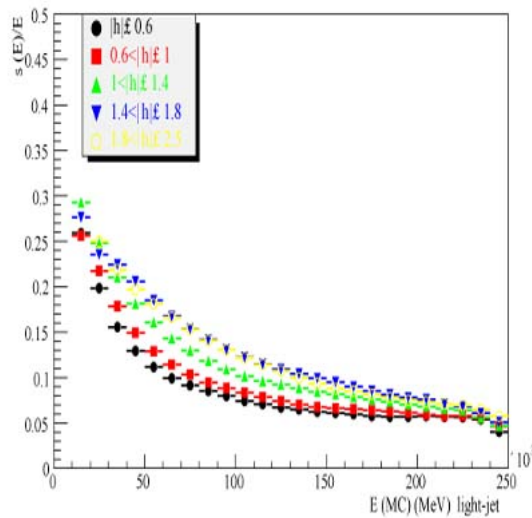


Figure 19: Energy jet resolution for different $\eta$ ranges.

26

**b–jets energy calibration** :

Energy calibration of $b$–jets has been performed by studying the ratio of the reconstructed $b$–jet energy over the corresponding initial (*i.e.* before any gluon radiation) $b$ quark. Some of the $b$–quarks will decay semileptonically ($b \to \ell\bar{\nu}c$) with the neutrino undetected. If the lepton is an electron, it will be, most of the time, merged in the jet energy; if it is a muon, it is not contained in the calorimeter and is reconstructed in the muon spectrometer. In the present algorithm, the muon is not added so the muon energy is missing in the jet energy. Since the muon is reconstructed, we can identify such events and calibrate them separately[11]. The distribution of the distance $\Delta R$ between the $b$–jet and the closest reconstructed muon is shown in figure 20: the $b$–decay is tagged as muonic if $\Delta R$ is smaller than 0.2.
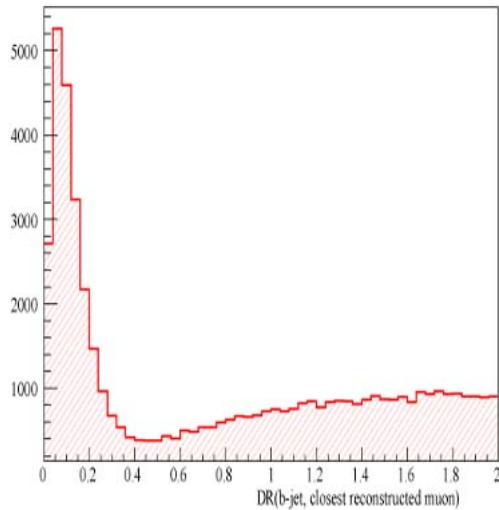


Figure 20: Distance $\Delta R$ between a $b$–jet and the closest reconstructed muon.

Figure 21 shows the ratio between the $b$–jet reconstructed energy and the corresponding $b$–quark energy as a function of the $b$–quark energy, in five $\eta$ ranges and for both kinds of $b$ decays. The calibration for muonic $b$ decays is clearly different from the other $b$ decays. The calibration factors, function of energy and defined for each range in $\eta$, are extracted from these curves. Figure 22 shows the same variables, after calibration, for any $\eta$ value and any kind of $b$–decay: the miscalibration is smaller than 2%.

---

[11]We did not try to identify electrons in $b$–jets and to calibrate the corresponding jet separately.
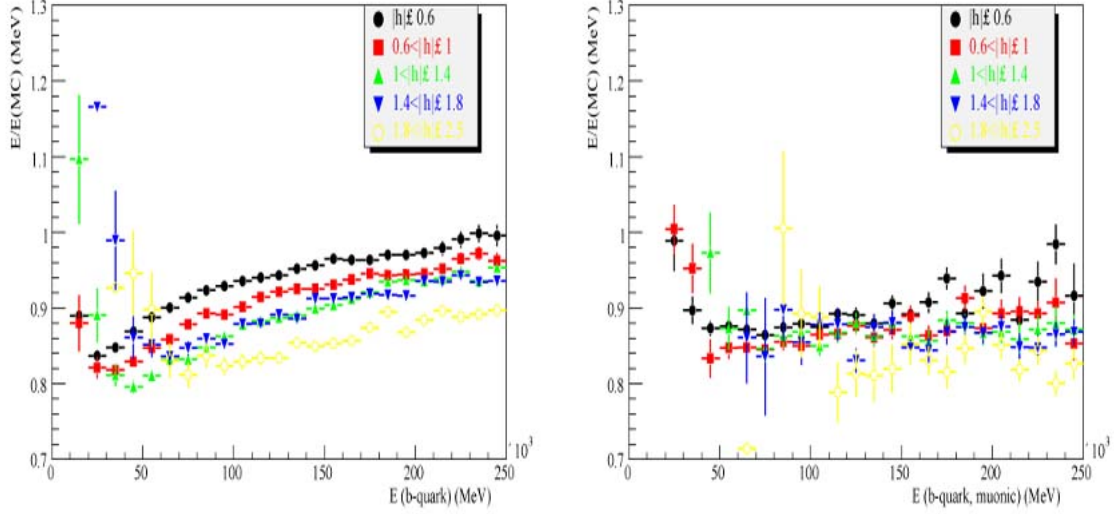
Figure 21: Left: ratio between the reconstructed $b$–jet energy and the corresponding $b$–quark energy, as a function of the $b$–quark energy and for different ranges in $\eta$, for non muonic $b$–decays. Right: same plot for muonic $b$–decays.
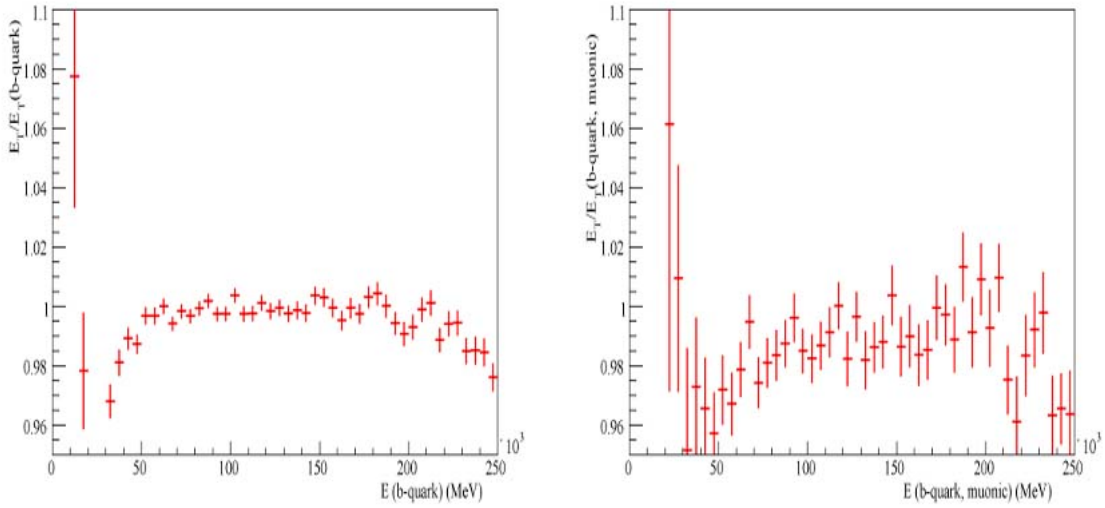


Figure 22: Check of the $b$–jet energy calibration.

## 4.2 Electron reconstruction

Electromagnetic clusters are reconstructed with the sliding window algorithm. It searches amongst all cells of the electromagnetic calorimeter for the window where the total energy is maximum. The window can be adjusted to different sizes, so that it can be optimized for different particles/energies. They are then corrected for different modulation effects, and longitudinal weights are computed to further optimize resolution and linearity. A cluster of size $\Delta\eta \times \Delta\phi = 5 \times 5^{12}$ is created.

High–$p_T$ electrons are searched by associating tracks to sliding–window clusters, and computing shower–shape variables, track–to–cluster association variables, and TRT hits variables. Dedicated track–fitting procedures for electrons are being developed. More details are provided in section 5 which deals with the electron/jet separation needed to reduce background from QCD multijet events in $t\bar{t}$ analysis.

Figure 23 shows the electron identification efficiency of $t\bar{t}$ events as a function of the transverse momentum. The obtained efficiency, for electrons with reconstructed $p_T > 20$ GeV is $\sim 70\%$.
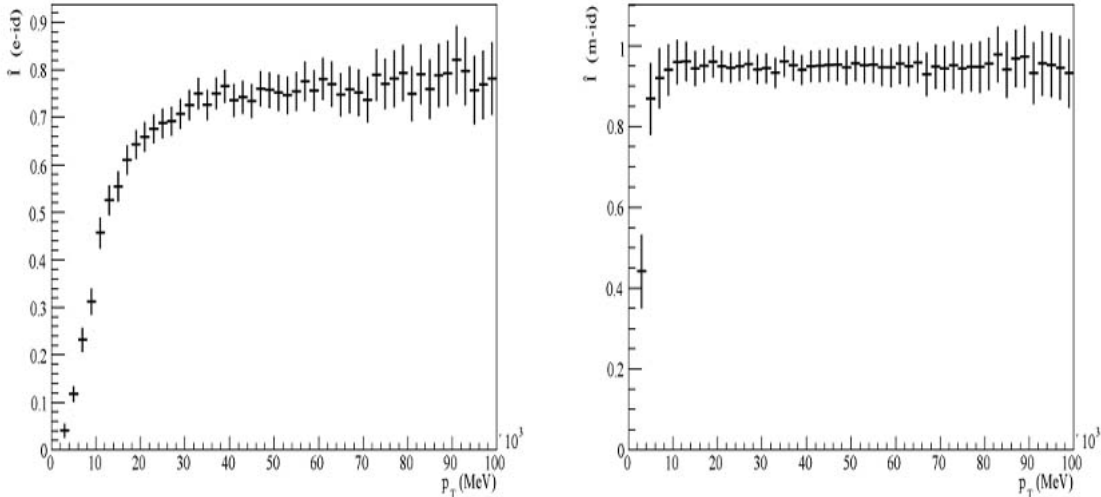


Figure 23: Electron (left) and muon (right) identification efficiency of $t\bar{t}$ events as a function of the transverse momentum.

## 4.3 Muon reconstruction

Muon measurement and identification is optimized according to the $p_T$ regimes. High–$p_T$ muons ($> 100$ GeV) are measured by extrapolating the muon–spectrometer track parameters in the muon spectrometer inward through the calorimeters and inner tracker to the interaction point. Combination with the optimum inner–detector track may also be done. The extrapolation of the muon trajectory to the inner–tracker track allows computation of the energy loss through the intervening material. Energy–loss parameterizations can be applied to correct the track momenta, as determined at the muon–spectrometer entrance, to the final–state muon momenta at the interaction point. Furthermore, direct

---

$^{12}$We recall that the size of the electromagnetic cells in the second sampling is $0.025 \times 0.025$.

measurement of catastrophic energy loss (important at high $p_T$ ) can be used to correct the muon momentum.

For muons in the 6–100 GeV $p_T$ range, momentum determination is performed by both systems. The muon spectrometer provides a flag that uniquely identifies the muon. For momenta below 30 GeV, the measurement resolution derives mostly from the inner tracker as the muon–spectrometer resolution is dominated by multiple Coulomb scatters.

In the following the "MuonBoy" algorithm is used[**?**]. Figure 23 shows the efficiency of the muon identification algorithm as a function of the transverse momentum on signal events. The identification efficiency is ∼90% for $p_T > 20$ GeV/c. The purity of the muon sample is ∼95% (signal).

## 4.4   Missing $E_T$

At hadron colliders, the initial energy of the colliding partons along the beam axis is not known (because the energy of each parton is split, and constantly exchanged between its constituents), so the amount of missing energy cannot be determined. However, the initial energy of the particles traveling transverse to the beam is zero, so any net momentum in the transverse direction indicates missing transverse energy.

Missing $E_T$ is reconstructed from the energy deposed in all calorimeter cells and from the reconstructed muons. A correction is applied for the energy lost in the cryostat between the electromagnetic and hadronic calorimeters.

Figure 24 shows the missing $E_T$ reconstructed in $Z \rightarrow e^+e^-$ events where no neutrino is present that is when no $E_T^{miss}$ is expected and also on top events in the lepton plus jets channel where one neutrino is present and so where $E_T^{miss}$ is expected. Clearly a cut above 20–25 GeV would remove events without expected $E_T^{miss}$.
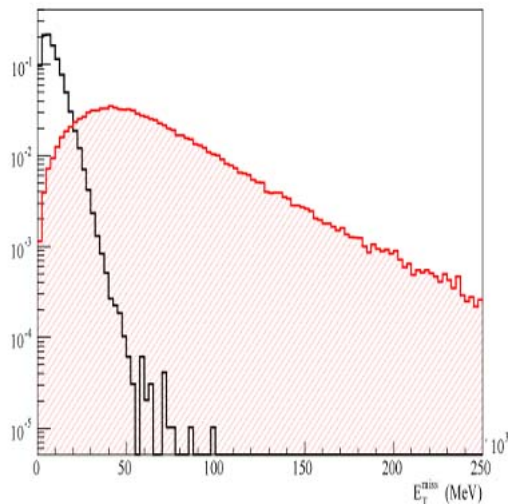


Figure 24: Distribution of missing $E_T$ for $Z \rightarrow e^+e^-$ and top events decaying in lepton plus jets.

# 5    Fighting against reducible background: electron / jet separation

The identification of isolated high transverse momentum electrons ($p_T \geq 25$ GeV/c) is essential for physics studies at the LHC. Typical examples are the searches for decays of the Higgs boson into four electrons $H \rightarrow ZZ^{(*)} \rightarrow 4e$, with a cross section $\sim 0.2$ fb for a Higgs mass of 130 GeV/$c^2$, the production of Z with decays $Z \rightarrow e^+e^-$ ($\sigma = 1.5 \times 10^{-6}$ mb), or the production of $W$ with decays $W \rightarrow e\nu$ ($\sigma = 1.5 \times 10^{-5}$ mb). The QCD di–jet cross section being of the order of 1 mb, to obtain an inclusive electron signal, a rejection factor $\sim 10^5$ is required on QCD jets. Moreover as detailed previously; the reducible background of our analysis in the $t\bar{t}$ events in the lepton plus jets channel can be strongly reduced by such a requirement.

For the separation of electrons from jets, discriminating variables are defined, based on both the calorimeters and the inner tracking system. Cuts on these variables are developed to maintain high electron efficiency. The thresholds applied on these cuts can vary with the transverse momentum but also with the pseudorapidity. Indeed electromagnetic shower shapes are sensitive to the amount of material in front of the calorimeter. The description of the detector is changing for each major Data Challenge in order to be closer and closer to the detector "as–build". Thus it is necessary to re–optimize these thresholds for the new CSC data.

The following sections describe such optimization performed on single electrons at various energies and electrons from $Z \rightarrow e^+e^-$. The electron identification efficiency is studied using these samples. Performance are also studied regarding the jet rejection capability of the electron identification algorithm. A sample of QCD dijets is used for that. The procedure follows prescription detailed in [**?**].

## 5.1    Selection criteria

### 5.1.1    Trigger selection

The electron trigger includes two menu items: the single object menu em25i and the double object menu 2em15i. The first letter stands for the physics object, in this case for an electromagnetic one, the second one is the transverse energy for which the trigger is efficient, and the last letter $i$ indicates an isolation requirement.

The LVL1 and LVL2 trigger information are not available in the data format we are using. As detailed in [**?**] the LVL1 would select $\sim 95\%$ of electrons. At the Event Filter level electrons are selected based on the cluster transverse energy $E_T$ and shower shape quantities that distinguish isolated electromagnetic objects from jets. Selection criteria are very similar to the one used in the offline analysis, but the thresholds are looser than in the offline analysis. The $E_T$ threshold is 20 GeV for the single object trigger menu and 12.5 for the double trigger menu.

In the following trigger selection will not be used except the selection on the transverse energy measurement.

### 5.1.2    Offline Analysis

The offline electron/jet separation procedure consists in using the calorimeter information to select events containing a high–$E_T$ electromagnetic shower. Then, a good quality track is selected and required to match the electromagnetic calorimeter shower in $(\eta, \phi)$ as

well as in the energy–momentum reconstruction. Finally the TRT information is used to improve the identification of electrons.

As detailed previously, the inclusive dijet sample includes prompt photon events, quark bremsstrahlung, $W$, $Z$ and top production. These events are vetoed in this analysis. A part of the dijet sample contains electrons originating from heavy flavor decays. They are also vetoed for this particular study on the determination on the rejection capability on QCD–jets of the electron identification algorithm. To reject them the following procedures are used. Events coming directly from a quark might have a small vertex radius. Thus an electron which has a radius, based on Monte Carlo truth information, smaller than 10 mm is considered as a signal one and is therefore not considered in the analysis.

**Use of calorimeter information** : EGAMMAREC is an algorithm designed to calculate quantities used to separate electrons and photons from jets. In the electromagnetic calorimeter electrons are narrow objects, while jets tend to have a broader profile. Hence, shower shapes can be used to reject jets.
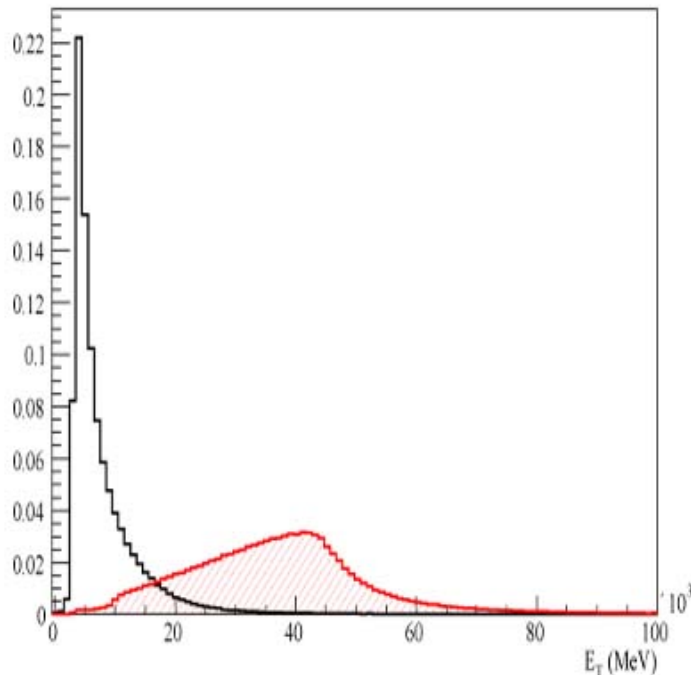


Figure 25: $E_T$ distribution of all clusters in each event after in the electromagnetic calorimeter for electrons from Z events (hatched histogram) and for jets (empty one).

This is handled by the EMSHOWERBUILDER tool which calls a number of algorithms that calculate diverse quantities using information from the first and second samplings of the electromagnetic calorimeter, as well as the first sampling of the hadronic calorimeter. Figure 25 shows the distribution of the transverse energy of electromagnetic clusters reconstructed for electrons from Z and pions from jets.

**Hadronic leakage** : Electromagnetic showers deposit a small amount of energy in the hadronic calorimeter, typically less then 2% for electrons, either due to their low energy, as

in this study, or because of the presence of the cryostat wall for more energetic electrons. The hadronic leakage is defined as the ratio of the transverse energy reconstructed in the first compartment of the hadronic calorimeter in a window $\Delta\eta \times \Delta\phi = 0.2 \times 0.2$ to the transverse energy reconstructed in the electromagnetic calorimeter. This ratio is shown in figure 26 for electrons and jets.
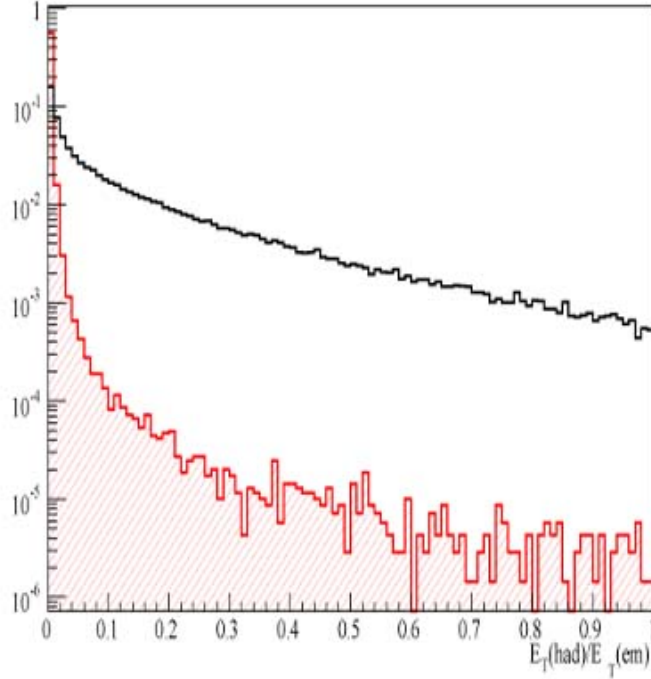


Figure 26: Hadronic leakage, defined as the ratio of the transverse energy reconstructed in a window $\Delta\eta \times \Delta\phi = 0.2 \times 0.2$ in the first compartment of the hadronic calorimeter to the transverse energy in the electromagnetic calorimeter. The distributions are shown for jets (empty histogram) and electrons (full histogram) at low luminosity. Only the $E_T$ trigger selection is applied beforehand. The distributions are normalised to unit area.

**Use of the second compartment of the ECAL** : Electromagnetic showers deposit most of their energy in the second sampling of the electromagnetic calorimeter. The following variables are used in the second sampling of the electromagnetic calorimeter:

- Electrons deposit most of their energy in a $\Delta\eta \times \Delta\phi = 3 \times 7$ window (in units of cells). The lateral shower shape, $R_\eta(37)$, is given by the ratio of the energy reconstructed in a $3 \times 7$ cluster by the energy in a $7 \times 7$ cluster. This variable (*cf.* figure 27 on left) shows a peak near one for electrons because of the very small lateral leakage; large tails ar lower values of $R_\eta(37)$ for the jets are expected.

- The lateral width (*cf.* figure 27) is calculated with a window of $3 \times 5$ cells using the energy weighted sum over all cells, which depends on the particle impact point inside the cell: $\omega_{\eta 2} = \sqrt{\frac{\sum E_c \times \eta^2}{\sum E_c} - \left(\frac{\sum E_c \times \eta}{\sum E_c}\right)^2}$
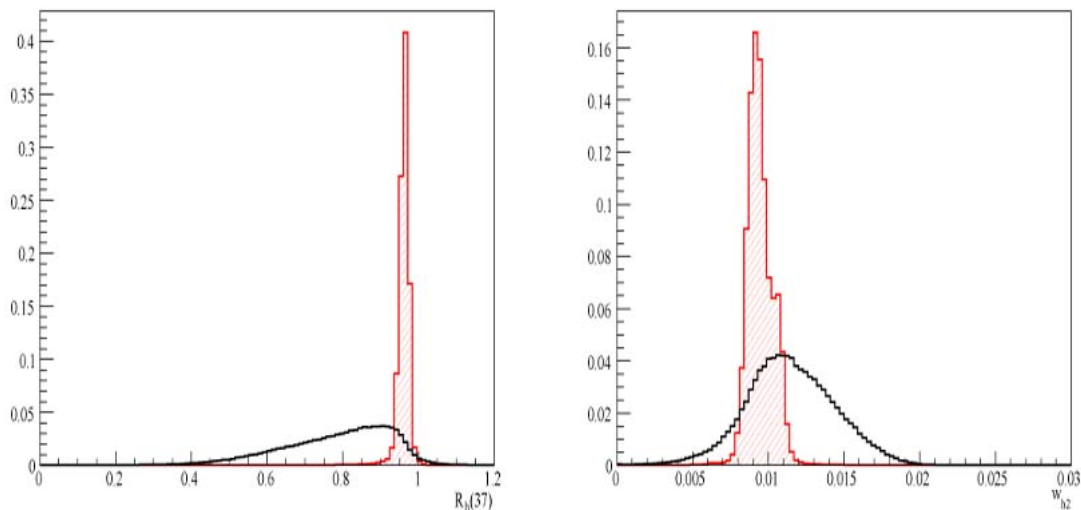
Figure 27: Lateral shower shape $R_\eta(37)$ (left) and lateral width $\omega_{\eta 2}$ (right). The distributions are shown for jets (empty histogram) and electrons (full histogram) at low luminosity. Only the $E_T$ trigger selection is applied beforehand. The distributions are normalised to unit area.

**Use of the first compartment of the ECAL** : Cuts applied on the variables used in the hadronic calorimeter and the second sampling of the electromagnetic calorimeters reject jets with energetic pions and wide showers; jets with single or multiple $\eta$, $\pi^0$, etc., are now the main contribution which can fake the electrons. The first compartment with its very fine granularity in rapidity can be used to detect substructures within a shower and thus isolated $\pi^0$'s and $\gamma$'s can be discriminated against efficiently. The lateral shower shape in the strips is exploited when a minimal amount of energy (0.5%) is reconstructed in the strips and for $|\eta| < 2.35$ where the strips granularity is fine enough. For all first compartment criteria, two cells in $\phi$ are summed.

- Jets with $\pi^0$ decays are found to have often two maxima. The shower is studied in a window $\Delta\eta \times \Delta\phi = 0.125 \times 0.2$ around the hottest cell to look for a second maximum. If more than two maxima are found the second highest maximum is chosen. Two variables are used:

  - The difference $\Delta E = E_{max2} - E_{min}$ of the energy associated with the second maximum $E_{max2}$ and the energy reconstructed in the strip with the minimal value between the first and second maximum $E_{min}$ (*cf.* figure 28 on the left).
  - $\Delta E_{max2} = E_{max2}/(1 + 9 \times 10^{-3}E_T)$, with $E_T$ the transverse energy of the cluster in the electromagnetic calorimeter and the constant value 9 refers to low luminosity. To ensure not to be sensitive to fluctuations, the value of the second maximal energy deposit has to be greater than a threshold which depends linearly on the transverse energy (*cf.* figure 28 on the right).

- The total shower width is determined in a window $\Delta\eta \times \Delta\phi = 0.0625 \times 0.2$ corresponding typically to 40 strips in $\eta$. It is calculated from: $\omega_{tot1} = \sqrt{\Sigma E_i \times (i - i_{max})^2 / \Sigma E_i}$, where $i$ is the strip number and $i_{max}$ the strip number of the first local maximum. This width is shown for electrons and jets in figure 29.
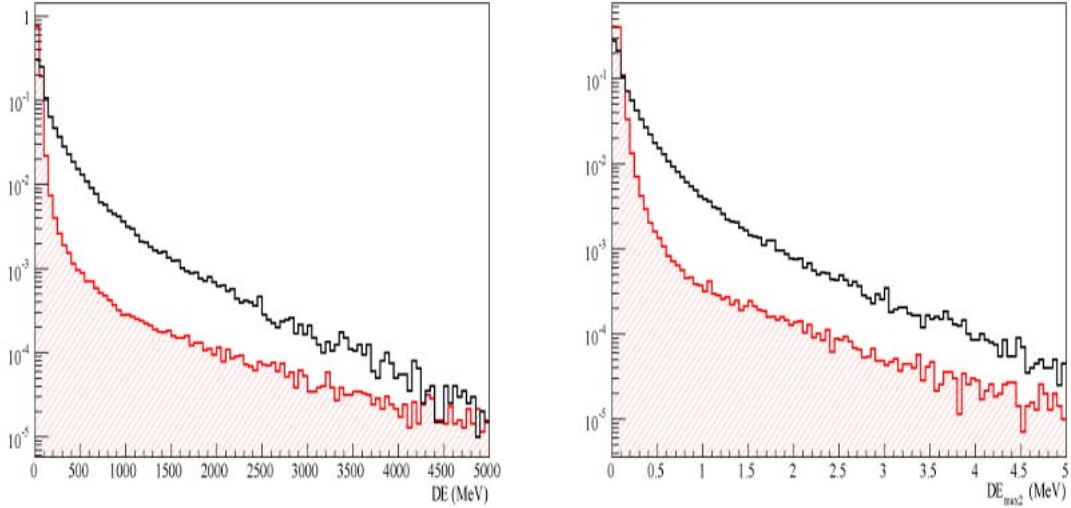
Figure 28: Left: Difference $\Delta E$ of the energy of the second maximum $E_{\mathrm{max2}}$ and the energy reconstructed in the strip with the minimal value between the first and second maximum ($E_{\mathrm{min}}$). Right: $\Delta E_{max2}$. The distributions are shown for jets (empty histogram) and electrons (full histogram) at low luminosity. Only the $E_T$ trigger selection is applied beforehand. The distributions are normalised to unit area.
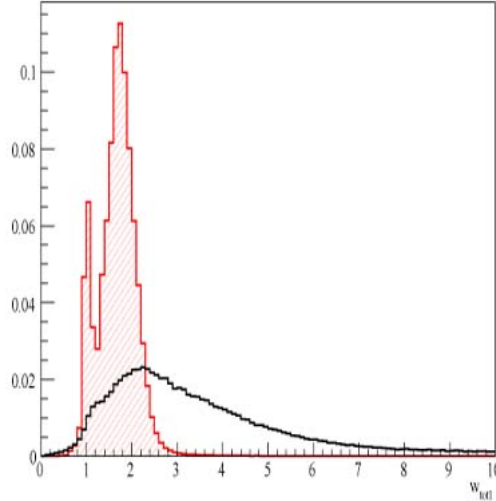


Figure 29: Total shower width $\omega_{tot1}$ in the first compartment of the electromagnetic calorimeter. The double peak structure for electrons reflects the varying granularity in the end–caps of the electromagnetic calorimeter. The distributions are shown for jets (empty histogram) and electrons (full histogram) at low luminosity. Only the $E_T$ trigger selection is applied beforehand. The distributions are normalised to unit area.

After these cuts only very narrow showers with one reconstructed maximum remain. The two following variables are used for a fine study of the shower shape:

- $F_{side}$ giving the shower shape in the shower core is shown in figure 30 on the left. It is calculated with the following formula: $F_{side} = [E(\pm 3) - E(\pm 1)]/E(\pm 1)$, where

35

$E(\pm n)$ is the energy in the $\pm n$ strips around the strip with highest energy.

- The shower width using three strips around the one with the maximal energy deposit is shown in figure 30 on the right. It is given by the following formula: $\omega_{3strips} = \sqrt{\Sigma E_i \times (i - i_{max})^2 / \Sigma E_i}$, where $i$ is the number of the strip and $i_{max}$ the strip number of the most energetic one. This variable can help for some particular $\eta$ bins.



Figure 30: Shower shape $F_{side}$ in the shower core (left) and shower width in 3 strips $\omega_{3strips}$ (right), of the first compartment of the electromagnetic calorimeter. The distributions are shown for jets (empty histogram) and electrons (full histogram) at low luminosity. Only the $E_T$ trigger selection is applied beforehand. The distributions are normalised to unit area.
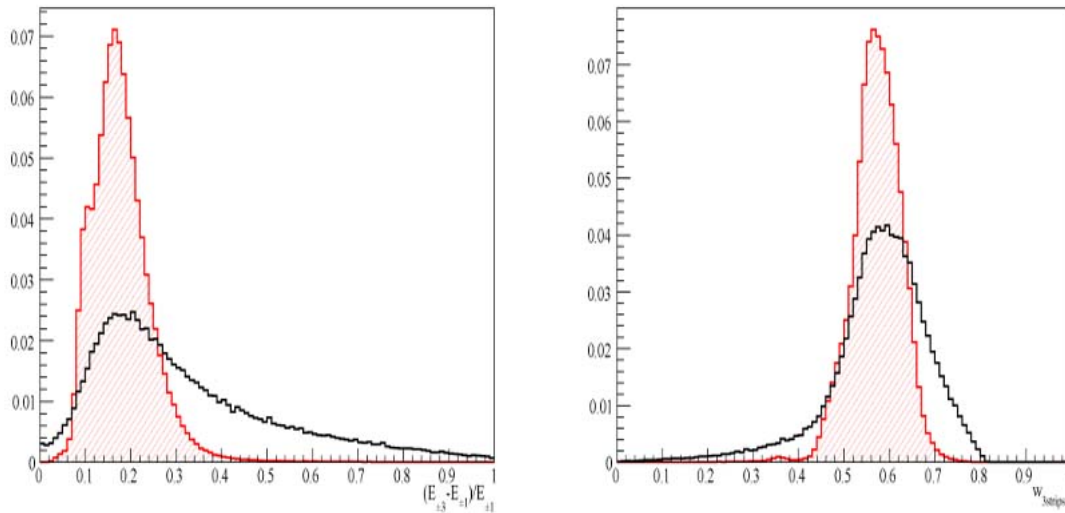
Figure 31 shows the average values of the calorimeter–based discriminating variables used for electron/jet separation as a function of the pseudo–rapidity. Since these variables are pseudorapidity dependent, the threshold values are tuned in several intervals. These subdivision is motivated by the varying granularities, lead thickness and material in front of the electromagnetic calorimeter. The first two bins, $(0, 0.8)$ and $(0.8, 1.37)$, cover the barrel of the electromagnetic calorimeter. The crack in the calorimeters between $1.37 < |\eta| < 1.52$ is excluded from the analysis. In the end–caps, the intervals are $(1.52, 1.8)$, $(1.8, 2.0)$, $(2.0, 2.35)$ and $(2.35, 2.47)$, essentially determined by the varying granularity in the first sampling. The quantities calculated using the first compartment can be used only in the regions $|\eta| < 1.37$ and $1.52 < |\eta| < 2.35$ since outside these regions the granularity in the first compartment is (too) coarse.

Figure 32 shows the average values of the calorimeter–based discriminating variables used for electron/jet separation as a function of the transverse momentum.

The cuts on the variables are tuned to obtain an efficiency independent of the pseudorapidity $\eta$. Thresholds are defined to be as close as possible to the edge of the electron distributions. Thus there is not a big loss of efficiency compared to the EF level, but the gain in the rejection of jets could be important. In some cases, like for $\omega_{3strips}$, the EF cuts are kept. For variables being highly correlated other tunings would be possible.

Figure 31: Distributions of the mean of each calorimetric discriminating variable as a function of the pseudo–rapidity $|\eta|$ for electrons (circle) and jets (triangle).

**Use of Inner Detector information** : After the calorimeter cuts, the contamination of the inclusive signal from charged hadrons is greatly reduced. The remaining background is dominated by photon conversion and low multiplicity jets containing high–$p_T$ $\pi^0$ mesons. It can be reduced further by requiring the presence of a good quality track pointing to an electromagnetic cluster with a good energy–momentum match.

Cluster and track information are combined in the EMTRACKMATCHBUILDER of the EGAMMAREC algorithm. Only tracks with $p_T > 5$ GeV/c are kept. An angular matching
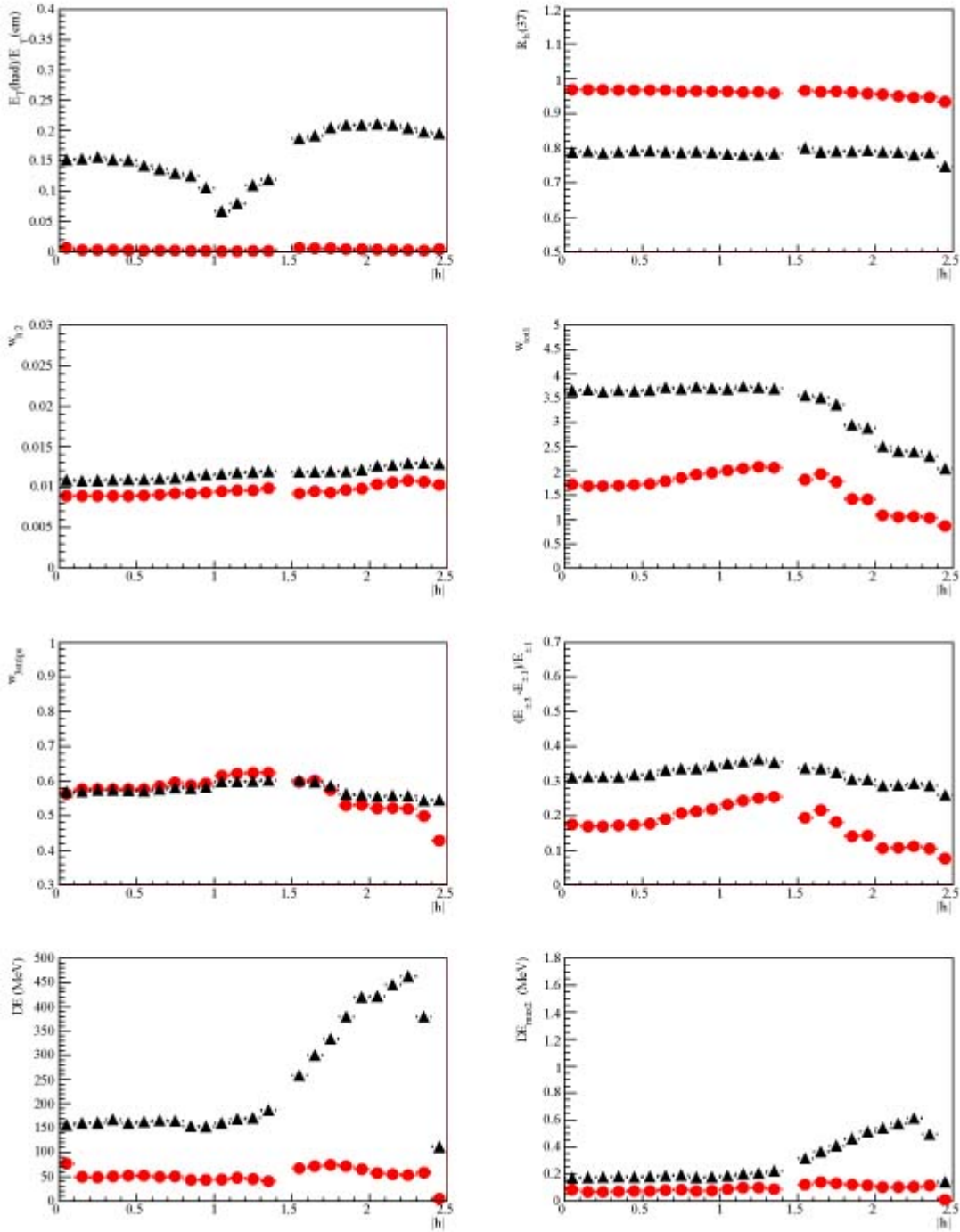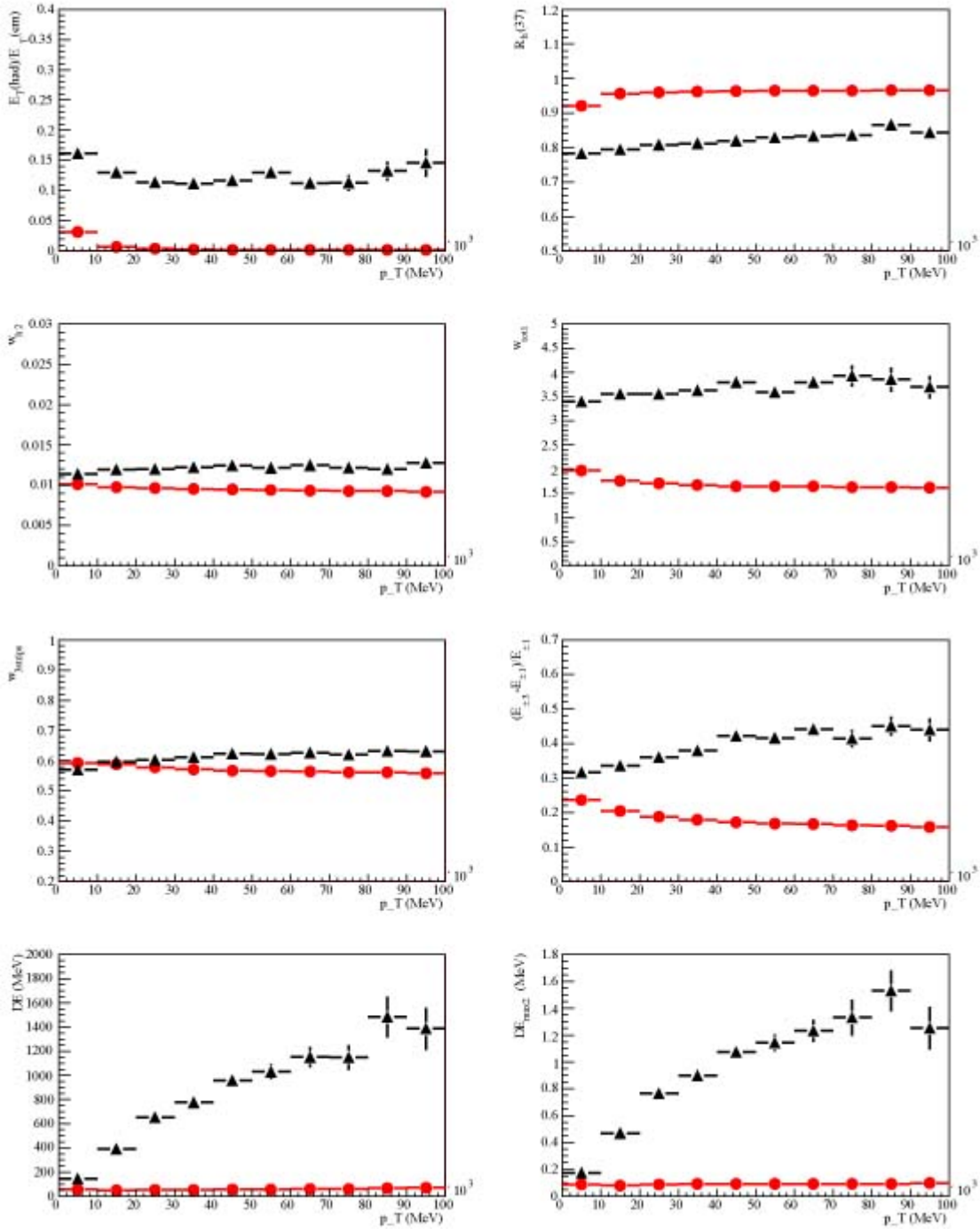
Figure 32: Distributions of the mean of each calorimetric discriminating variable as a function of the transverse momentum $p_T$ for electrons (circle) and jets (triangle).

is done in a window $\Delta\eta = \pm 0.05$, $\Delta\phi = \pm 0.1$ between the selected electromagnetic clusters and the position of the track extrapolated to the calorimeter. In case more than one track is found, the one with the highest $p_T$ is retained. If the $E/p$ ratio is less than 4, the track matching is successful. In the subsequent particle identification step the information provided by EGAMMAREC can be used. A set of track quality cuts are at first applied, referred as ID–cuts:

- at least nine precision hits (Pixel+SCT);

- at least two hits in the pixels, one of which being in the b–layer;

- a transverse impact parameter $|A_0| < 0.1$ cm.

**Use of the Inner Detector/calorimeter matching information** : The jet rejection can be significantly improved by ensuring consistency between the electromagnetic calorimeter and the Inner Detector information. First, the angular matching between the track and the electromagnetic cluster is checked (*cf.* figure 33):

- $|\eta| = |\eta_{cluster}^{strips} - \eta_{ID}|$, where $\eta_{cluster}^{strips}$ is computed in the first sampling of the electromagnetic calorimeter, where the granularity is very fine, and $\eta_{ID}$ is the pseudorapidity of the track extrapolated to the calorimeter;

- $|\phi| = |\phi_{cluster}^{strips} - \phi_{ID}|$, where $\phi_{cluster}^{strips}$ is computed in the second compartment of the electromagnetic calorimeter and $\phi_{ID}$ is the azimuth of the track extrapolated to the calorimeter;
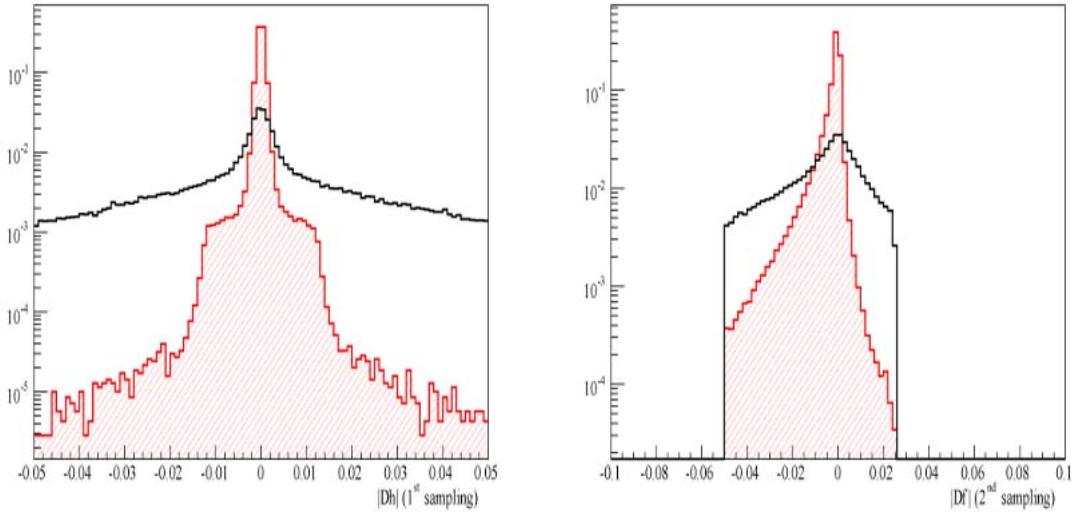


Figure 33: Angular matching between charged tracks extrapolated to the electromagnetic calorimeter and electromagnetic clusters in pseudorapidity ($|\Delta\eta|$) and azimuth ($|\Delta\phi|$). The distributions are shown for jets (empty histogram) and electrons (full histogram) at low luminosity. Only the $E_T$ trigger selection is applied beforehand. The distributions are normalised to unit area.

Subsequently, the energy $E$ measured in the electromagnetic calorimeter is compared to the momentum $p$ measured in the Inner Detector (*cf.* figure 34 on the left). In the case of an electron, the momentum should match the energy. Still, large tails at low and high values of the ratio can be seen. These are due to conversion electrons as well as soft bremsstrahlung.

Typically it is required that $0.9 < E/p < 2.5$ in the barrel and $0.9 < E/p < 3.5$ in the end–cap[13]

---

[13]These thresholds are 0.7 in the standard algorithm.

**Use of transition radiation in the TRT information** : A further reduction of the charged hadron contamination is obtained by rejecting tracks having a low fraction of high–threshold TR hits. Figure 34 (right) shows the ratio $N_{TR}/N_{straw}$ between the number of high threshold hits $N_{TR}$ and the total number of TRT hits $N_{straw}$. Thresholds applied at the TRT level for TDR analysis were defined in $p_T$ and $\eta$ bins, but were not tuned ever since.
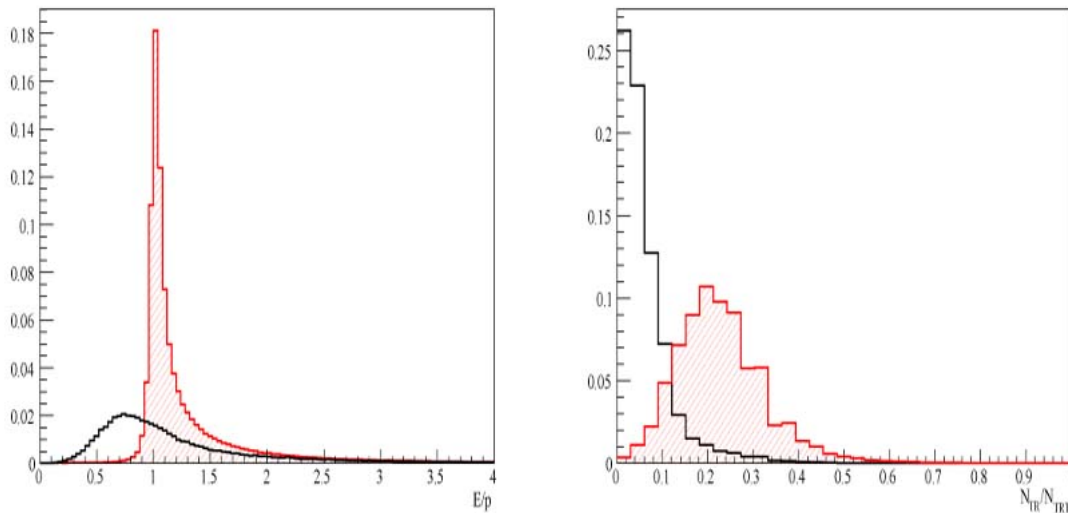


Figure 34: Ratio $E/p$ between energy of the electromagnetic clusters to momentum of reconstructed charged tracks (left) and ratio $N_{\mathrm{TR}}/N_{\mathrm{straw}}$ (right). The distributions are shown for jets (empty histogram) and electrons (full histogram) at low luminosity. Only the $E_T$ trigger selection is applied beforehand. The distributions are normalised to unit area.

## 5.2  Electron identification performance

The identification of a candidate cluster/track as originating from a signal electron is based on the sequence of criteria described above. The total identification efficiency $\varepsilon_e$ is defined as:

$$\varepsilon_e = \frac{N_e^t}{N_e},$$

where $N_e$ is the number of electron particles, from the Monte Carlo truth block of the combined ntuple, with $p_T > 5$ GeV/c and an angular matching in a window $\Delta\eta = \pm 0.05$, $\Delta\phi = \pm 0.1$ between the selected electromagnetic clusters and the position of the particle. $N_e^t$ is the number of electrons identified after all analysis cuts.

Table 4 shows the efficiencies obtained for electrons from $Z$ over the full rapidity range $|\eta| < 2.47$. The crack in the calorimeters between $1.37 < |\eta| < 1.52$ is excluded. Results are presented for optimised and standard selection thresholds. The total efficiency $\varepsilon_e$ is $\sim 71\%$ for optimised while being $\sim 73\%$ for standard. The lower efficiency in the presented analysis is due essentially to the tighter cuts applied on $E/p$ variable. This is reflected in figure 35 which shows the electron identification efficiency as a function of the pseudo–rapidity and the transverse momentum.

| $\varepsilon_e$ (in %) | standard | optimized |
|:---:|:---:|:---:|
| Calo | $93.9 \pm 0.1$ | $94.2 \pm 0.1$ |
| ID | $83.0 \pm 0.1$ | $82.7 \pm 0.1$ |
| ID–Calo | $82.8 \pm 0.1$ | $78.7 \pm 0.1$ |
| TRT | $73.4 \pm 0.1$ | $70.6 \pm 0.1$ |

Table 4: Electron identification efficiency $\varepsilon_e$ of the offline analysis on electrons from Z for standard cuts and for optimized cuts as detailed above. The crack in the electromagnetic calorimeter, between $1.37 < |\eta| < 1.52$, is not taken into account.
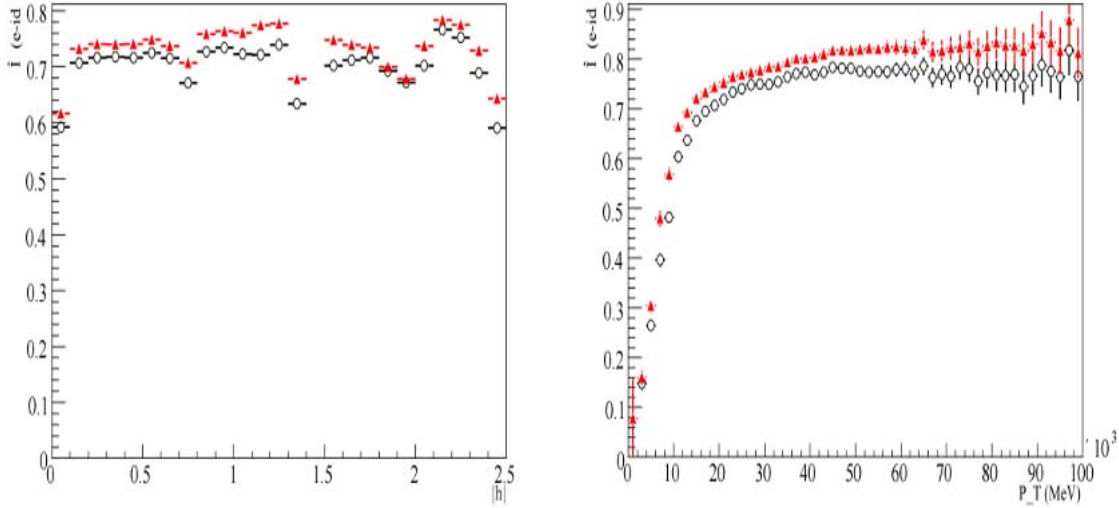


Figure 35: Electron identification efficiency for $Z$ events as a function of the pseudo–rapidity (left) and the transverse momentum (right). Standard performance are represented by full triangles while the ones obtained in this study are represented by open circles.

## 5.3 Jet rejection

Events which do not pass the LVL1 are immediately rejected: at least one region of size $\Delta\eta \times \Delta\phi = 0.12 \times 0.12$ must be found, in which the summed transverse energy of all stable particles except muons and neutrinos is at least 17 GeV. Only 8.33% of all generated events are accepted and then fully simulated.

The normalization of the rejection is done with respect to the number of jets, reconstructed with the fast simulation program ALTFAST, above 20 GeV. The files of full simulation used in this analysis are not complete as they passed the particle filter described above. A total of $N_i = 86400$ events are present after particle filter, corresponding to a fraction of $\varepsilon_f = 8.33\%$ of all generated events. The true number of initial events is then $N_i/\varepsilon_f$. The number of initial jets $N_{jets}$ is determined on a subset of events and are summarised in table 5. These numbers are based on the study of $N_{tot} = 2 \times 10^6$ dijet events, before particle filtering. The normalization factor is then $N_{jets}/N_{tot}$. The total number of initial jets used in this study is thus given by: $N_{jet}^i = \frac{N_i \times N_{jets}}{\varepsilon_f \times N_{tot}}$. The rejection factor $R(\text{jet})$ of QCD–jets is defined by the ratio of initial jets $N_{jet}^i$ over the number of mis–identified

41

jets $N_{jet}^{res}$:

$$R(jet) = \frac{N_{jet}^{i}}{N_{jet}^{res}}$$

| $|\eta|$ | $N_{\text{jets}}$ | | | |
|---|---|---|---|---|
| | low luminosity | | high luminosity | |
| | $E_T > 17$ (GeV) | $E_T > 22$ (GeV) | $E_T > 25$ (GeV) | $E_T > 27$ (GeV) |
| $\eta| \leq 0.80$ | 407546 | 186543 | 126680 | 97735 |
| $0.80 < |\eta| \leq 1.37$ | 272738 | 142704 | 94506 | 76020 |
| $1.37 < |\eta| \leq 1.52$ | 65658 | 31365 | 20000 | 1629 |
| $1.52 < |\eta| \leq 1.8$ | 123606 | 58978 | 37070 | 31488 |
| $1.8 < |\eta| \leq 2.0$ | 88604 | 42149 | 26212 | 21643 |
| $2.0 < |\eta| \leq 2.35$ | 48304 | 69275 | 44198 | 35888 |
| $2.35 < |\eta| \leq 2.47$ | 89760 | 23037 | 14720 | 11882 |

Table 5: Number of initial jets based on the analysis of $2 \times 10^6$ ($6 \times 10^5$) dijet events at low (high) luminosity, before particle level filtering.

Table 6 shows the rejection factors of QCD jets obtained after each step of the analysis. The rejection after the Calorimeter level is $\pm 1600$ in good agreement with previous analyses. Unfortunately, the statistics avalaible for this analysis are much less than in [?] where $N_i \sim 1.1 \times 10^6$. Thus there are not enough statistics to apply all selection criteria. The obtained rejection is $\sim 20000$ but with very large uncertainties.

| $\varepsilon_e$ (in %) | standard | optimised |
|---|---|---|
| Calo | $1212 \pm 62$ | $1560 \pm 90$ |

Table 6: Rejection of jets by the offline electron identification algorithm for standard cuts and for optimised cuts as detailed above. The crack in the electromagnetic calorimeter, between $1.37 < |\eta| < 1.52$, is not taken into account.

Still, these results are in agreement with the ones obtained by [?]. A jet rejection larger than $10^5$ can be expected on QCD–jets. Thus the background for "top in leptons plus jets" analysis, coming from jets misidentified as electrons can be considered as negligible.

# 6 Top events selection without calibration and b-tagging

As the top quarks are abundantly produced at the LHC, the question which can be raised is "how well can we observe the top quark with a not–yet optimal detector performance?". In order to answer to this question, first we investigate whether we can do top physics analysis without $b$–jet tagging.

The experimental signature for top events includes one or more $b$–tagged jets, originating from the decay of the top quark. Thus, the $b$–tagging performance of the ATLAS detector has an important role in top analysis. An efficient $b$–tagging needs precise alignement of the trackers of the Inner Detector, which will be reached only after few months of data taking.

This study explores the possibility of reconstructing top events in $t\bar{t}$ production assuming the absence of $b$–tagging. We follow prescription as described in [?] and [?] on the lepton plus jets channel, in the hadronic mode.

## 6.1 Selection of events

The event selection ($t\bar{t} \rightarrow \ell\nu b j j b$ ($\ell = e, \mu$)) proceeds in two steps: a preselection is first performed in order to remove part of the fully hadronic $t\bar{t}$ decays and the semileptonic decays with too small jet or lepton energy (background events). The final selection is then performed on the remaining events.

### 6.1.1 Preselection

The following cuts are applied:

- The missing transverse energy $E_T^{miss}$ must be greater than 20 GeV.

- There must be at least one reconstructed lepton with transverse momentum greater than 20 GeV/c and $|\eta| < 2$.

- There must be at least four jets with $|\eta| < 2.5$ and transverse energy greater than 30 GeV.

Table 7 shows the number of events in the signal and in the background samples after each step of the selection.

| cut | signal | background | efficiency (%) |
|-------|--------|------------|----------------|
| none | 101467 | 111022 | 100 |
| final | 2097 | 386 | 1.2 |

Table 7: Number of events after each cut of the filter.

### 6.1.2 Final selection

As explained in [?], in order to reduce fully hadronic events selected because of a leptonic decay of one of the $b$ quarks, the number of isolated leptons (with $p_T > 30$ GeV/c and $|\eta| < 2.5$) is required to be exactly one, with a lepton being declared isolated if the distance
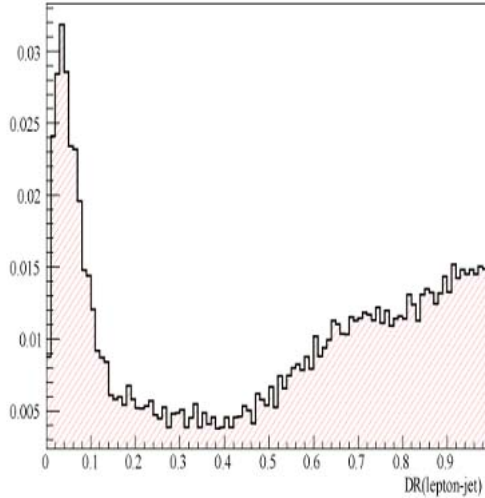
Figure 36: Distance between the leptons and the closest jet.

to the closest (non–electron) jet is greater than 0.2. Figure 36 shows the distribution of the distance between the electrons or the muons and the closest jet.

All four permutations of three jets (out of the four selected jets) are considered. For each permutation the jets are added together and the transverse momentum of the system is determined. The permutation which results in the highest value of $p_T$ is taken as the set of jets that correspond to the decay of the top quark.

### 6.1.3   Selection of the light jets

Using this sample, it is also possible to reconstruct the $W$–boson of the top quark decay, that itself decays hadronically into two jets.

For this we take the three jets that constitue the top quark, and select two jets that originated from the $W$–decay. All three permutations of selecting two jets out of three are considered, and again the combination taken is that which results in the highest value of $p_T$ of the summed two jets. The $W$–boson mass is then the invariant mass of the two jet system.

In figure 37 this mass distribution is shown for different jet $p_T$ cuts. Table 8 shows the number of $W$'s, background events, and signal to background ratio, in these histograms.

For a jet $p_T$ cut of 20 GeV/c the $W$–boson peak is almost invisible due to the peak in the background close to this threshold; the signal to background ratio is only 0.6. For a jet $p_T$ cut of 30 or 40 GeV/c the $W$–boson peak around 80 GeV starts to be visible with a signal to background ratio reaching $\sim 5$.

In the following a set of "best $W$–matched" events is selected by requiring $50 < M_{jj} < 90$ GeV/$c^2$.

## 6.2   Top mass measurement

The top mass is simply reconstructed as the invariant mass of the three selected jets. Figure 38 shows the expected top signal for a luminosity of 100 $pb^{-1}$, *i.e.* after a few days of LHC running. The most important background contribution, production of W

44

| Jet $p_T$ cut | all events | | | $50 < M_W < 90$ GeV/$c^2$ | | |
| --- | --- | --- | --- | --- | --- | --- |
| | $N_W$ | $N_{bkg}$ | S/B | $N_W$ | $N_{bkg}$ | S/B |
| 20 | 6473 | 13945 | 0.5 | 3365 | 5460 | 0.6 |
| 30 | 4112 | 1166 | 3.5 | 2137 | 475 | 4.5 |
| 40 | 2306 | 549 | 4.2 | 1122 | 216 | 5.2 |

Table 8: Number of W and background events, and signal to background ratio, in the histograms of figure 37.
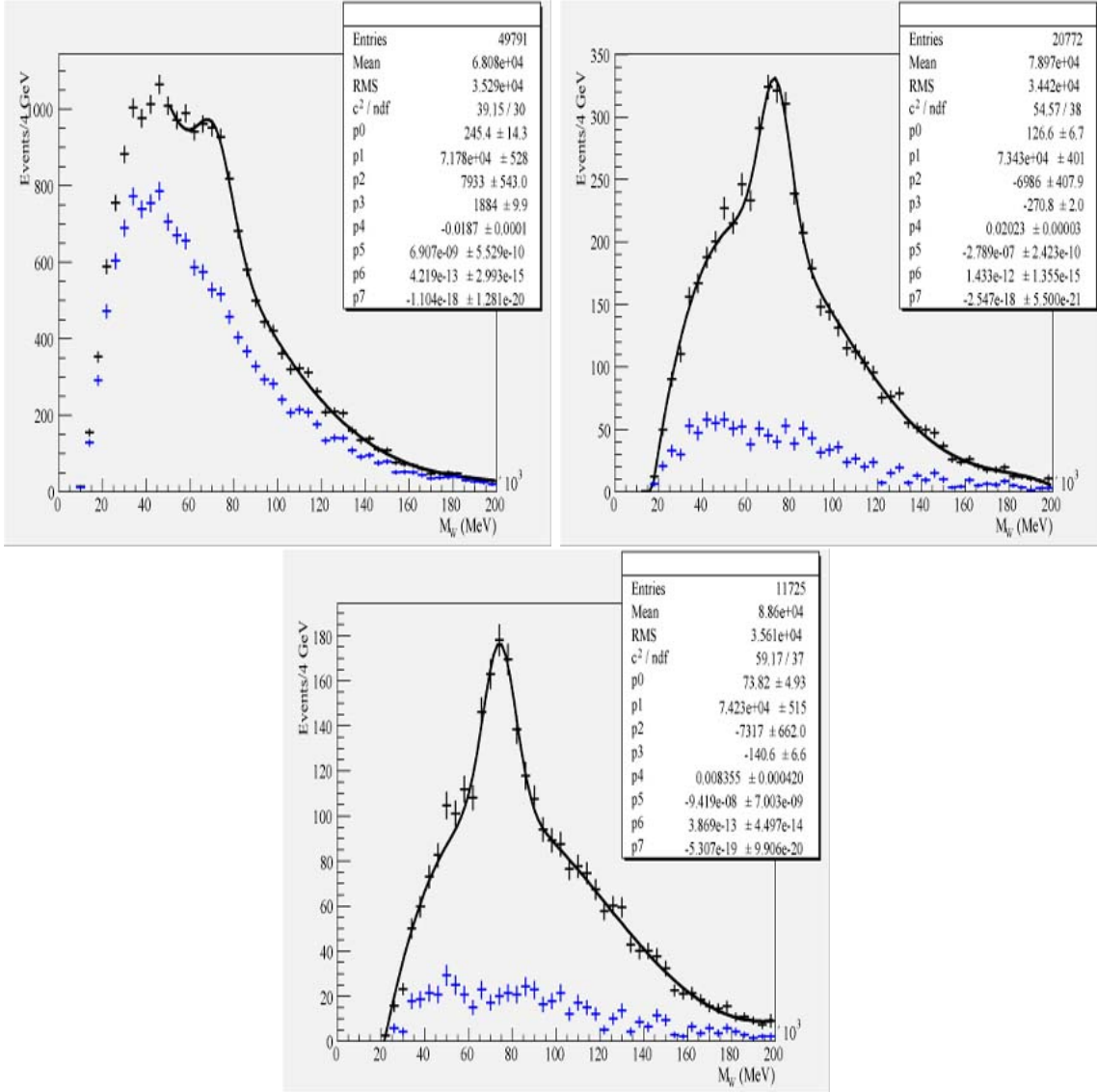


Figure 37: Invariant mass of the two light jets with a jet $p_T$ cut of 20 GeV/c (left), 30 GeV/c (middle) and 40 GeV/c (right). Full histograms represent background distributions and hatched signal distributions.

+ 4 jets, is shown as hatched histogram. The top mass peak is clearly visible above the combinatorial background and the very smooth distribution of the W + 4 jets events. A fit is performed on this distribution with a gaussian for the signal together with a third order polynomial for the background. The mean value being fitted is 169.8 ± 0.6

GeV. The width of the distribution is $\sim 17$ GeV/$c^2$. A total of 2097 events enter the signal distribution, and 385 are considered as background events. This leads to an overall efficiency of $\sim 2\%$ and signal to background ratio of $S/B \sim 5$. Table 9 shows the number of signal and background events for other jet $p_T$ cuts.
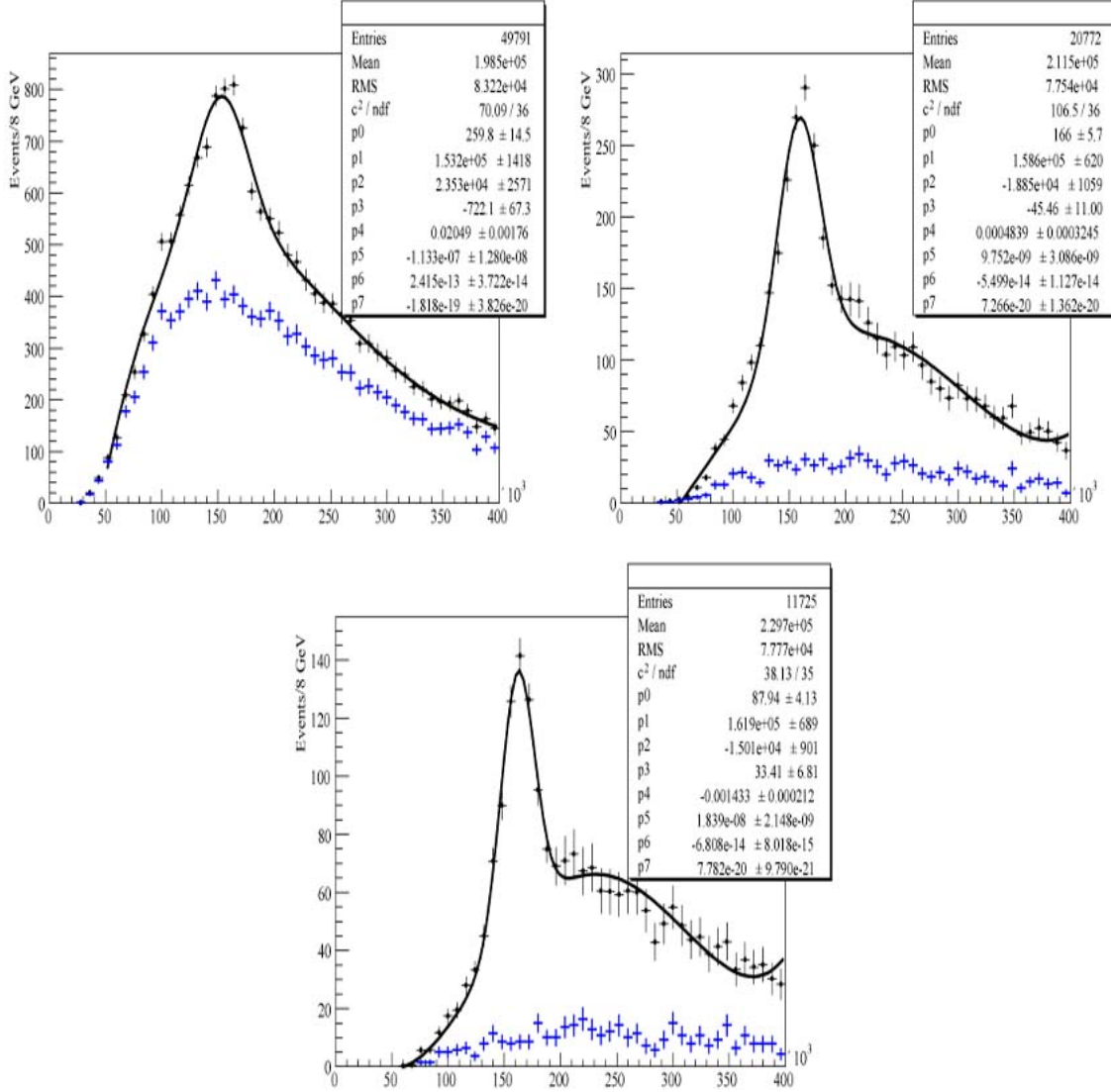


Figure 38: Invariant mass of the three jets with a jet $p_T$ cut of 20 GeV/c (left), 30 GeV/c (middle) and 40 GeV/c (right). Full histogram represents background distribution

| Jet $p_T$ cut | all events | | | $50 < M_W < 90$ GeV/$c^2$ | | |
|---|---|---|---|---|---|---|
| | $N_{top}$ | $N_{bkg}$ | S/B | $N_{top}$ | $N_{bkg}$ | S/B |
| 20 | 3721 | 5663 | 0.6 | 2108 | 1998 | 1.0 |
| 30 | 2097 | 386 | 5.4 | 1267 | 144 | 8.8 |
| 40 | 944 | 136 | 6.9 | 609 | 54 | 11.1 |

Table 9: Number of top and background events, in the mass range $100 < M_{top} < 220$ GeV/$c^2$, and signal to background ratio in the histograms of figures 38 and 39.
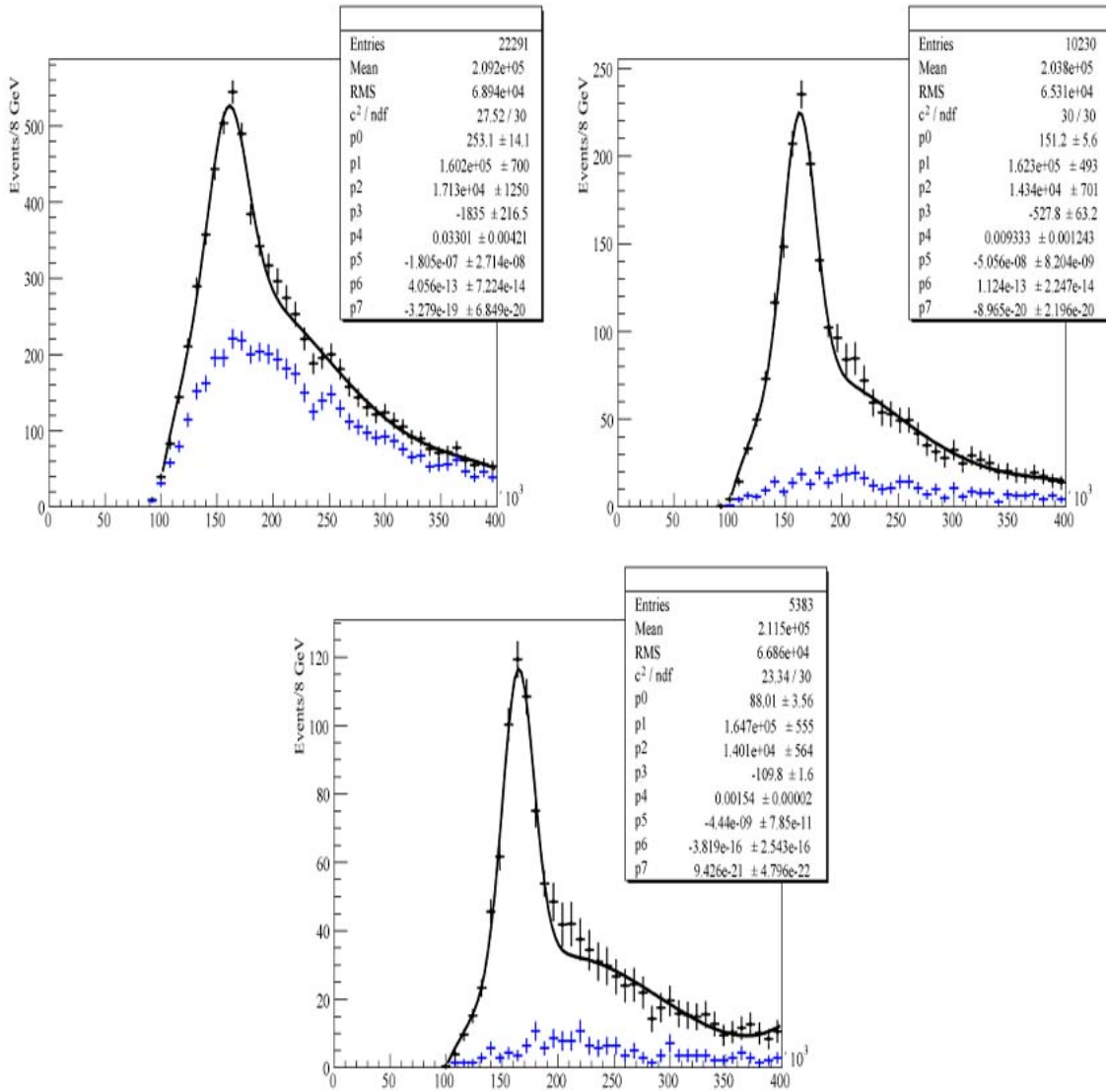
Figure 39: Invariant mass of the three jets with a jet $p_T$ cut of 20 GeV/c (left), 30 GeV/c (middle) and 40 GeV/c (right) for those whose $W$ reconstructed mass is between 50 and 90 GeV/$c^2$. Full histogram represents background distribution

When considering only those events for which the $W$ reconstructed mass is between 50 and 90 GeV/$c^2$, one obtains the distribution of figure 39. A total of 1267 events enter the signal distribution, and 144 are considered as background events. This leads to an overall efficiency of 1.2% and signal to background ratio of $S/B \sim 9$. The mean value being fitted is $169.6 \pm 0.5$ GeV. The width of the distribution is $\sim 19$ GeV/$c^2$.

The fact that the top quark mass peak is clearly visible, and can be fitted separately from the background, allows to perform the top–mass measurement and cross section determination without $b$–tagging. Even if the normalisation and shape of the background is rather different (but still smooth) these parameters can be determined. It is this behavior that gives confidence we can perform this measurement using the first ATLAS data already after 2–3 days of data taking.

# 7 Analysis using b–tagging information

The scenario with no available $b$–tagging is pessimistic, certainly after some initial running period. Therefore we also investigate the behaviour of the top mass reconstruction if we use $b$–tagging. The following shows a study of the mass measurement in the lepton plus jets channel, in the hadronic mode, after a week of data taking at low luminosity (*i.e.* integrated luminosity of 300 $pb^{-1}$). We follow prescription as detailed in [?].

## 7.1 Selection of events

The event selection ($t\bar{t} \rightarrow \ell\nu bjjb$ ($\ell = e, \mu$)) proceeds in two steps: a preselection is first performed in order to remove part of the fully hadronic $t\bar{t}$ decays and the semileptonic decays with too small jet or lepton energy (background events). The final selection is then performed on the remaining events.

### 7.1.1 Preselection

The following cuts are applied:

- The missing transverse energy must be greater than 20 GeV.

- There must be at least one reconstructed lepton with transverse momentum greater than 20 GeV/c and $|\eta| < 2$.

- There must be at least four jets with $|\eta| < 2.5$ and transverse energy greater than 30 GeV.

| cut | signal | background | efficiency (%) |
|-----|--------|-----------|----------------|
| none | 101467 | 111022 | 100 |
| final | 1604 | 22 | 1.6 |

Table 10: Number of events after each cut of the filter.

### 7.1.2 Final selection

The final selection proceeds as follows:

- As explained in [?], in order to reduce fully hadronic events selected because of a leptonic decay of one of the $b$ quarks, the number of isolated leptons (with $p_T > 20$ GeV/c and $|\eta| < 2$) is required to be exactly one, with a lepton being declared isolated if the distance to the closest (non–electron) jet is greater than 0.2.

- In the case of the analysis using the $b$–tagging information, there must be exactly two $b$–jets with $p_T > 20$ GeV/c and $|\eta| < 2.5$.

Table 10 shows the number of events in the signal and in the background samples after each step of the selection.

The top quark's mass is determined from the reconstruction of the invariant mass of a three–jet system: the two light jets from the $W$ and one of the two $b$–jets. The determination of this combination of three jets proceeds in two steps: the choice of the two light

48

jets, explained in section 7.2.1, and the choice of the $b$–jet associated to the reconstructed hadronic $W$, explained in section 7.3.1. The top mass reconstruction obtained is described in section 7.3.2, and a non–exhaustive study of systematic errors on this measurement is detailed in section 7.3.3.

## 7.2  Hadronic $W$ reconstruction

### 7.2.1  In situ jet energy calibration

Events kept after the selection described above have at least two light jets above a given threshold on their transverse momentum. Figure 40 (left panel) shows the distribution of the invariant mass of the light jet pairs made with events with only two light jets.
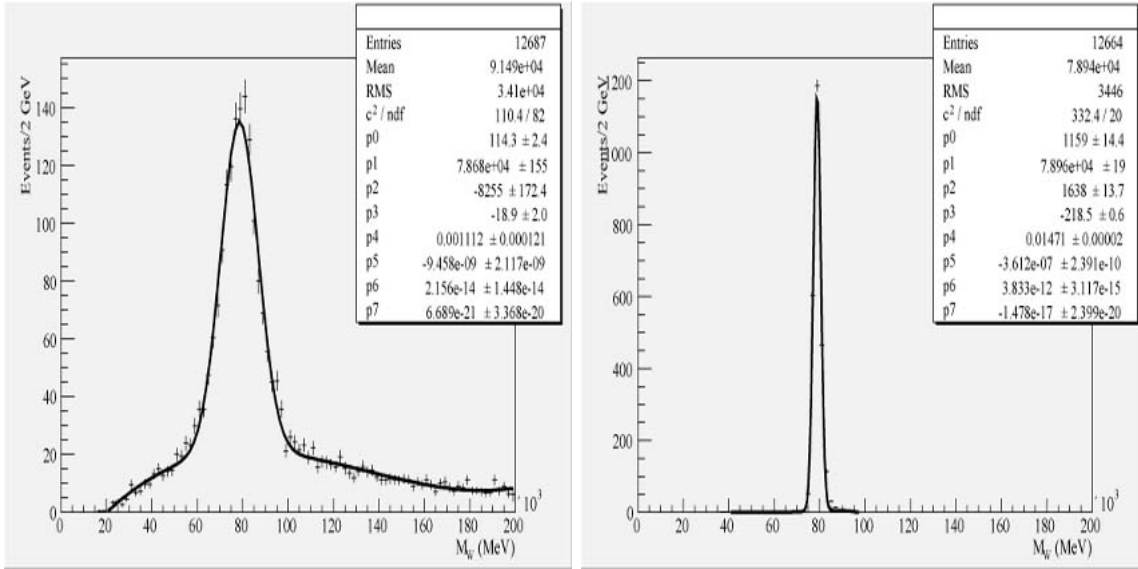


Figure 40: Invariant mass of the two light jets before (left) and after (right) jet energy in situ rescaling.

The accuracy of the top mass measurement is strongly correlated to the precision of the jet energy reconstruction (*cf.* [?]). In order to reduce the incidence of a light–jet energy mis–measurement (due to the energy loss out of cone) on the precision of the top mass measurement, an in–situ calibration of these jets is performed, through a $\chi^2$ minimization procedure. This minimization is applied event by event, for each light jet– pair combination. The expression of the $\chi^2$, given by the equation below, is the sum of three terms: the first (and leading) one corresponds to the constrain of the jet pair invariant mass $M_{jj}$ to the PDG $W$ mass ($M_W$); the others correspond to the jet energy correction factors, $\alpha_i$ with $i = 1, 2$, to be determined by this minimization ($\sigma_i$ is the resolution on the light jet energy determined as explained previously).

$$\chi^2 = \frac{(M_{jj} - M_W)^2}{\Gamma_W^2} + \frac{(E_{j_1}(1 - \alpha_1))^2}{\sigma_1^2} + \frac{(E_{j_2}(1 - \alpha_2))^2}{\sigma_2^2}$$

The $\chi^2$ is minimized, event by event, for each light jet pair; the light jet pair $j_1 j_2$ corresponding to the minimal $\chi^2$ is kept as the hadronic W candidate. This minimization procedure leads to the corresponding energy correction factors $\alpha_1$, $\alpha_2$.

49

### 7.2.2  $W$ mass reconstruction

The hadronic $W$ mass, reconstructed with the light jets chosen by the $\chi^2$ minimization, is therefore very narrow, as illustrated in right panel of figure 40, since, given the jet energy resolution, the first term dominates the $\chi^2$. Further on, we consider only the hadronic $W$ candidates which belong to a mass window of $\pm 3\Gamma_{m_W}$ ($\Gamma_{m_W} = 2.1$ GeV).

## 7.3  Top reconstruction

### 7.3.1  Choice of the $b$–jet associated to the hadronic $W$

The next step in the top mass reconstruction is to associate one of the two $b$–jets in the event to the hadronic $W$ candidate. The chosen algorithm is to take the leading $b$–jet to the highest $p_T$ for the reconstructed top.

### 7.3.2  Top mass measurement

**Top mass reconstruction** :
The reconstructed three jets (two light jets from the hadronic $W$ and the chosen $b$–jet) invariant mass is shown in figure 41. The mass peak ($170.9 \pm 0.8$ GeV/$c^2$) is in rather good agreement with the generated value ($175$ GeV/$c^2$); the width is equal to $\sim 14$ GeV/$c^2$.

In a mass window around $\pm 3\sigma_{m_{\text{top}}}$, a total of 1604 events enter the signal distribution, and 22 are considered as background events (*cf.* table 11). This leads to an overall efficiency of 1.6% and signal to background ratio of $S/B \sim 70$.
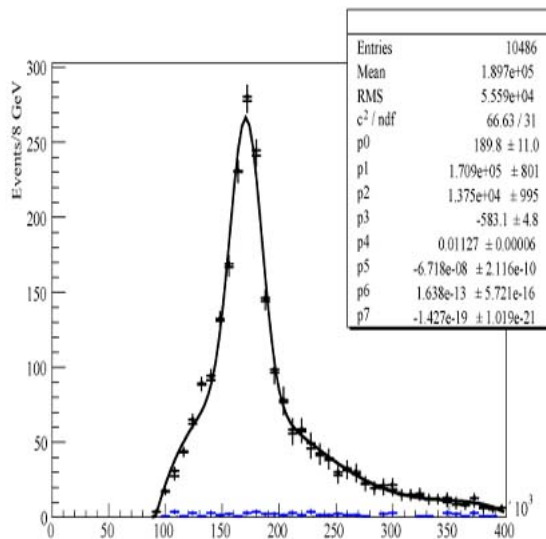


Figure 41: Invariant mass of the three jets with a jet $p_T$ cut of 30 GeV/c. Full histogram represents background distribution and hatched signal distribution.

### 7.3.3  Systematic errors

The results on the top quark mass measurement exposed above have been obtained with a jet cone size equal to 0.4 and a cut on the transverse momentum of the jets equal to 40 GeV/c.

| Jet $p_T$ cut | $N_{top}$ | $N_{bkg}$ | $S/B$ |
|---|---|---|---|
| 20 | 2709 | 61 | 44 |
| 30 | 1604 | 22 | 70 |
| 40 | 787 | 10 | 78 |

Table 11: Number of top and background events, in the mass range $130 < M_{top} < 210$ GeV/$c^2$, and signal to background ratio in histograms of figures 41 and 42.

$b$–**tagging** : The algorithm used for tagging the flavor of the jet is based on the Monte Carlo truth and has an efficiency $\sim 90\%$. A more realistic $b$–tagging algorithm is needed.

**Jet $p_T$ cut** : We have studied the variation of the reconstructed mass value as a function of the jet $p_T$ cut. Figure 42 shows the reconstructed top mass distribution obtained for these jet $p_T$ cuts. For a jet $p_T$ cut of 20 GeV/c, the reconstructed mass is $169.0 \pm 0.6$ GeV/$c^2$ with the width equal to $\sim 14$ GeV/$c^2$. For a jet $p_T$ cut of 40 GeV/c, the reconstructed mass is $172.5 \pm 1.0$ GeV/$c^2$ with the width equal to $\sim 11$ GeV/$c^2$.

The value of the reconstructed mass is systematically underestimated. This could be an effect of poor quality of the fit. As shown in figures 41 and 42 the summit of the mass peak is not well reproduced. Still it has been already reported in [**?**] that the reconstructed mass value shows a dependence with the cut on the jet energies due to resolution effects.

The choice between the various threshold values would have to be determined carefully by comparing the efficiency and purity obtained on signal and background samples.
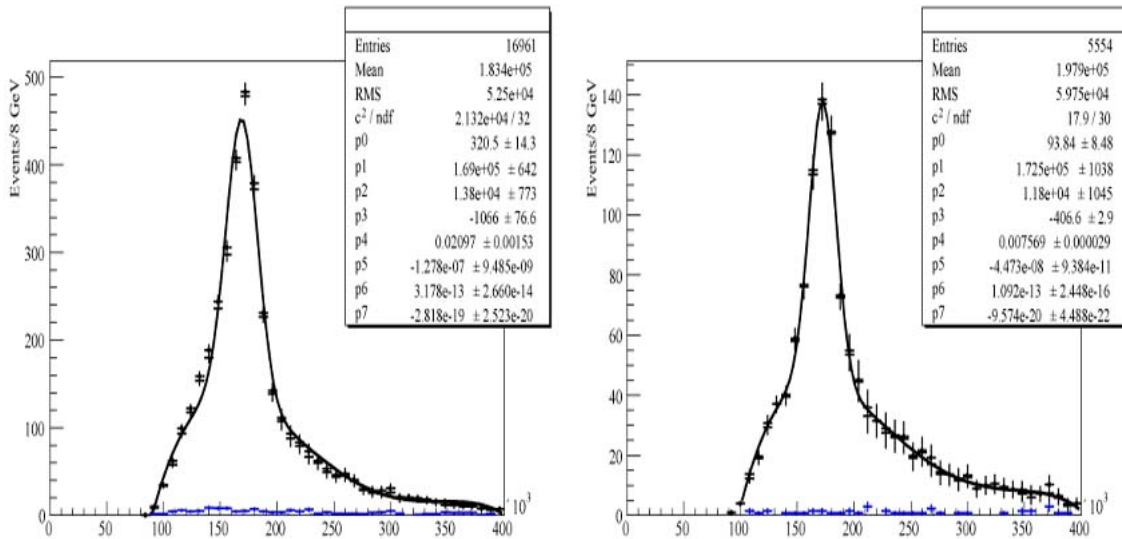


Figure 42: Invariant mass of the three jets with jet $p_T$ cuts of 20 GeV/c (left) and 40 GeV/c (right). The full histogram represents background distribution and the hatched one stands for signal distribution.

**Jet cone size** : A study could be performed with a different cone size (*e.g.* 0.7 instead of 0.4) for the jet definition. The energy calibration factors would have to be recalculated. By lack of time such study has not been performed.

$E_T^{\mathrm{miss}}$ **cut** : The $E_T^{\mathrm{miss}}$ cut applied (20 GeV), together with the request of one isolated lepton with a $p_T$ greater than 20 GeV leads to an important background rejection, according to the study performed in the ATLAS TDR[**?**]: therefore the $E_T^{\mathrm{miss}}$ cut is efficient enough. The sensitivity of this cut on our analysis has been evaluated for $E_T^{\mathrm{miss}} > 30$ GeV: an increase of its value does not affect strongly the reconstructed top mass measurement.

**Jet energy scale** : In order to estimate the effect of the jet energy scale uncertainty, a miscalibration coefficient would have to be applied to the $b$–jet and light jet energies. Because of lack of time this procedure has not been performed. Still we can use results obtained in [**?**]. A 1% scale error on $b$–jet energies would induce a shift on the top mass equal to 0.6 GeV. A 1% scale error on the light jet energies would induce a shift on the top mass equal to $\sim 0.2$ GeV.

# 8 Conclusion

We have studied the top quark mass reconstruction in the $t\bar{t} \to \ell\nu b j j b$ channel using full simulation (with a generated top mass of 175 GeV/$c^2$) and reconstruction of this process.

Both decays, leptonic ($\ell\nu b$) and hadronic ($j j b$), were considered for the selection.

During the commisioning phase of the ATLAS detector it will be crucial to understand the interplay between the top quark signal as a tool to improve the understanding of the detector ($b$–tagging, jet energy scale, particle identification...) and the top quark signal to perform precision measurements.

A study has been performed with hadronic decays which shows that in ATLAS the top quark can be easily reconstructed, even by using a very simple selection and without making any requirement in terms of $b$–tagging and jet energy reconstruction. The hadronically decaying $W$ boson can be reconstructed as well, giving an excellent handle on light jet energy calibration.

A more refined analysis is carried out after better understanding the detector and the data (in particular jet energy is calibrated and $b$–tagging is available). The mass reconstruction performance was studied. The electron/jet separation was studied in detail and it has been shown that the backgounrd coming from QCD–jets mis–identified as electrons is negligible. The study has been performed also taking into account background estimation from W + jets and it has been shown that once $b$–tagging is available this background becomes negligible. The resolution of the top mass is about 14 GeV/$c^2$. Therefore, the statistical error on the top mass after one week at $10^{33}$ $cm^{-2}$ $s^{-1}$ is 0.8 GeV/$c^2$. The statistical uncertainty will become negligible compared to the uncertainties related to the jet energy scale determination.

# References

[1] Cobal M. Bentveslen S. Top studies for the ATLAS detector commisioning, 2005. ATL-PHYS-PUB-2005-024.

[2] Tevatron July 2006 combination of CDF+D0 Run I+II results. http://www-cdf.fnal.gov/physics/new/top/top.html.

[3] Serfon C. Derue F. Electron/jet separation with dc1 data, 2005. ATL-PHYS-PUB-2005-0016.

[4] Schwindling J. Etienvre A-I., Meyer J-P. Top quark measurement in the lepton plus jets channel using full simulation, 2005. ATL-PHYS-INT-2005-022.

[5] Bordoni S. Selezione di eventi $t\bar{t}$ nell'esperianza ATLAS presso l'lhc, 2005. Tesi di Laurea Triennale.

[6] ATLAS collaboration. Tdr ATLAS detector and physics performance, vol. 1. *CERN/LHCC 99-14, ATLAS-TDR-14*, 1999.

[7] ATLAS collaboration. Tdr ATLAS detector and physics performance, vol. 2. *CERN/LHCC 99-15, ATLAS-TDR-15*, 1999.

[8] ATLAS Muon Saclay group. http://atlas-samusog.web.cern.ch/atlas-samusog/muonboy/muonboy.htm.